EarthArXiv Cover Sheet

Title

Coupled, decoupled, and abrupt responses of vegetation to climate across timescales

Authors

David Fastovich[1], Stephen R. Meyers[2], Erin E. Saupe[3], John W. Williams[4], Maria Dornelas[5,6], Elizabeth M. Dowding[10], Seth Finnegan[8], Huai-Hsuan M. Huang[9], Lukas Jonkers[10], Wolfgang Kiessling[7], Ádám T. Kocsis[7], Qijian Li[11], Lee Hsiang Liow[12], Lin Na[11], Amelia M. Penny[13], Kate Pippenger[14], Johan Renaudie[15], Marina C. Rillo[16], Jansen Smith[17], Manuel J. Steinbauer[18], Mauro Sugawara[19,20], Adam Tomašovỳch[21], Moriaki Yasuhara[22,23], Pincelli M. Hull[14,24,25]

Affiliations

*Corresponding Author: dfastovi@syr.edu
[1]Department of Earth and Environmental Sciences, Syracuse University, Syracuse, NY, USA
[2]Department of Geoscience, University of Wisconsin – Madison, Madison, WI 53706, USA
[3]Department of Earth Sciences, University of Oxford, South Parks Road, Oxford, OX1 3AN, United Kingdom
[4]Department of Geography & Center for Climatic Research, University of Wisconsin-Madison, 550 N. Park Street, Madison, WI 53706 USA
[5]School of Biology, University of St Andrews, St. Andrews, United Kingdom
[6]Guia Marine Lab, MARE, Faculty of Science of the University of Lisbon, 939, Estrada do Guincho, Cascais 2750-374, Portugal
[7]GeoZentrum Nordbayern, Friedrich-Alexander Universität Erlangen-Nürnberg (FAU), Erlangen, Germany
[8]Department of Integrative Biology & Museum of Paleontology, University of California, Berkeley, Berkeley, CA USA
[9]Smithsonian Tropical Research Institute, Panama
[10]Department of Geosciences, Princeton University, NJ, USA
[11]MARUM – Center for Marine Environmental Sciences University of Bremen, Bremen, Germany
[12]State Key Laboratory of Palaeobiology and Stratigraphy, Nanjing Institute of Geology and Palaeontology and Center for Excellence in Life and Paleoenvironment, Chinese Academy of Sciences, Nanjing, China
[13]Natural History Museum & Centre for Planetary Habitability, Department of Geosciences, University of Oslo, Oslo, Norway
[14]School of GeoSciences, University of Edinburgh, Edinburgh, United Kingdom
[15]Department of Earth and Planetary Sciences, Yale University, New Haven, CT, USA
[16]Museum für Naturkunde, Invalidenstraße 43, Berlin, Germany
[17]ICBM - Institute for Chemistry and Biology of the Marine Environment, University of Oldenburg, Wilhelmshaven, Germany
[18]Department of Earth & Environmental Sciences, University of Minnesota - Duluth, Duluth, MN, USA

[19]Bayreuth Center of Ecology and Environmental Research, University of Bayreuth, Bayreuth, Germany
[20]University of British Columbia, Vancouver, BC, Canada
[21]Mário Schenberg Institute, São Paulo, Brazil
[22]Earth Science Institute, Slovak Academy of Sciences, Bratislava, Slovakia
[23]School of Biological Sciences, Area of Ecology and Biodiversity, Swire Institute of Marine Science, Institute for Climate and Carbon Neutrality, Musketeers Foundation Institute of Data Science, The University of Hong Kong, Hong Kong, China
[24]State Key Laboratory of Marine Pollution, City University of Hong Kong, Hong Kong, China
[25]Yale Peabody Museum, 170 Whitney Ave, New Haven, CT, 06511, USA
[26]Swiss Federal Institute for Forest, Snow and Landscape Research, Birmensdorf, Switzerland

Corresponding Author

David Fastovich, dfastovi@syr.edu

Peer-review Statement

This manuscript has been submitted to *Science* and is not peer-reviewed. This preprint has been submitted to EarthArXiv. Subsequent versions of this manuscript may have slightly different content. If accepted, the final version of this manuscript will be available via the 'Peer-reviewed Publication DOI' link on the right-hand side of this webpage.

Abstract

Climate and ecosystem dynamics vary across timescales, but research into climate-driven vegetation dynamics usually focuses on singular timescales. We develop a spectral analysis-based approach that provides detailed estimates of the timescales at which vegetation tracks climate change, from 10^1 to 10^5 years. We report similarity of vegetation and climate even at centennial frequencies (149^{-1} to $18{,}012^{-1}$ years^{-1}). A breakpoint in vegetation turnover (797^{-1} years^{-1}) matches a breakpoint between stochastic and autocorrelated climate processes, suggesting that ecological dynamics are governed by climate across these frequencies. Heightened vegetation turnover at millennial frequencies ($4{,}650^{-1}$ years^{-1}) highlights the risk of abrupt responses to climate change, while vegetation-climate decoupling at frequencies >149^{-1} years^{-1} may indicate long-lasting consequences of anthropogenic climate change for ecosystem function and biodiversity.

Keywords

Spectral power continuum, community turnover, climate variability, dynamic equilibrium, non-linear ecological dynamics, temporal beta diversity, vegetation

Manuscript Text

Characterizing ecological dynamics across timescales is urgently required to understand how and at what rates ecosystems are likely to respond to anthropogenic climate change. Species and ecosystems differ in their responses to changing climates and these dynamics are timescale dependent (*1–4*). The climate system exhibits two interconnected modes of variability: short-term, stochastic, weather variations that scale to large, autoregressive, climate fluctuations at timescales longer than 100 to 1,000 years (*5*, *6*). Yet, most studies of climate-driven ecological dynamics have focused on narrow ranges of timescales (*7*).

Global networks of ecological and paleontological data (*8*, *9*) now enable us to characterize, in ways not previously possible, ecological responses to climate forcing across timescales and modes of climate variability. Former research has shown that fast ecological dynamics track climate change (*10*, *11*), while slow dynamics are lagged or decoupled from climate (*12–15*). Ecosystems can also linearly or nonlinearly respond to forcing, with the potential to lead to unexpected species' compositional changes (*16*).

Here, we focus on the relationships among temperature, precipitation, and vegetation compositional turnover in paleoecological records spanning hundreds to hundreds of thousands of years over the last 600,000 years. To quantify the coupling, decoupling, and scaling of climate drivers and ecological responses across timescales, we create and apply a conceptual and analytical framework rooted in spectral analysis (*17*). Whereas, many time series methods are only capable of examining vegetation-climate coupling at discrete temporal lags, in the frequency domain spectral analysis overcomes this limitation by comprehensively decomposing time series variability into specific timescales of observation. This decomposition is quantified in the power spectrum and provides insights into the relative contributions of different timescales to overall climate or vegetation variability.

Through this approach, we generate global power spectra of vegetation variability by averaging site-level power spectra for fossil pollen assemblages across a global compilation of 1,321 sites (*8*, *9*), with the densest coverage for the last 20,000 years (Fig. S1, Fig. S2). We compare these global vegetation compositional changes to power spectra of temperature and precipitation from a climate model simulation of the last 21,000 years (TraCE-21ka, Fig. S3, Fig. S4, Fig. S5, Fig. S6) (*18*, *19*). To capture lower-frequency climate variability, we include proxy temperature reconstructions that approximate global climate over the last two million years (*20*, *21*).

Paired Spectral Analysis of Climate and Vegetation: Analytical and Conceptual Framework

The exponential coefficient (β) of the power-law relationship ($S(f) \propto f^{-\beta}$) between spectral power (S) and frequency (f) defines the spectral continuum, quantifies how variance is partitioned across frequencies in power spectra of climate and ecological turnover, and identifies dynamic similarity between these systems across timescales (Fig. S7) (*22*, *23*). If vegetation composition changes in parallel with climate variability, the βs for vegetation should be similar to climate variability. For instance, a shift in low-frequency climate variability will induce a change in vegetation turnover at the same frequencies. However, the drivers of vegetation compositional change vary in relative importance across timescales (Fig. 1): disturbance, biotic interactions, and demographic processes are thought to be more important at short timescales; migration lags and other dispersal limitation, population dynamics, restriction to refugia, and ecosystem transformation dominate at intermediate timescales; and macroevolutionary processes such as speciation and extinction prevail on longer timescales (Fig. 1) (*1*, *2*). These processes modulate vegetation responses to climate and may cause the continuum of vegetation variability to diverge from climate ($\beta_{veg} \neq \beta_{clim}$).

We expect that matching βs for climate and vegetation are likely to emerge at intermediate frequencies (~$1{,}000^{-1}$ to $100{,}000^{-1}$ $years^{-1}$) given previous work (*10*, *11*) (Fig. 1). At these intermediate frequencies, the processes regulating assemblage composition can keep up with climate change (*10*, *11*) leading to $\beta_{veg} = \beta_{clim}$ (Fig. 1A). Across frequencies when $\beta_{veg} = \beta_{clim}$, we infer that vegetation is tracking climate and use the term 'fast tracking' (*11*), even though our methods do not test for causal links.

The relationship between climate and vegetation dynamics at lower (< $100{,}000^{-1}$ $years^{-1}$) and higher frequencies (> $1{,}000^{-1}$ $years^{-1}$) remains an open question, as does the frequencies at which the assumption of fast tracking no longer holds (*12*). High frequencies are particularly crucial for predicting vegetation responses to rapid, anthropogenic climate warming, as they examine how ecological and life-history factors may override the influence of climate variability. The vegetation response at high frequencies may be slow, because trees tend to have lifespans of 10^2 to 10^3 years (*24*), producing larger β in vegetation turnover than in climate (Fig. 1B, $\beta_{veg} > \beta_{clim}$). Conversely, disturbance through herbivory, fire, human land use, and disease could increase vegetation turnover at high frequencies decreasing β relative to climate (Fig. 1B, $\beta_{veg} < \beta_{clim}$) (*25*).

At low frequencies, vegetation dynamics distinct from intermediate and high frequencies may emerge. Climate tracking could persist, as expected at intermediate frequencies (Fig. 1C, $\beta_{veg} = \beta_{clim}$), or adaptive evolution could increase species' tolerances to new climate regimes (*26*), potentially reducing compositional responses to climate forcing. Consequently, vegetation turnover variability would increase minimally relative to climate variations (Fig. 1C, $\beta_{veg} < \beta_{clim}$). Conversely, if vegetation responses to environmental forcings are characterized by strong non-linearities (*16*, *27*), variability in vegetation turnover would be high relative to climate (Fig. 1C, $\beta_{veg} > \beta_{clim}$).

Spectral continuum of vegetation variability

To meaningfully compare climate and vegetation turnover we align their spatio-temporal characteristics through downsampling and low-pass filtering the climate model simulations (*28*). The proxy estimates of global climate variability cannot undergo this processing, resulting in spatiotemporal characteristics that differ from the fossil pollen records. We assess the effects of temporal uncertainty and uneven spatiotemporal coverage of the vegetation turnover data on the averaged power spectra (Fig. 2) by resampling sites and their corresponding posterior age estimates to produce an ensemble of power spectra, estimates of β, and estimates of the breakpoints in β (*28*). Lastly, we assess the sensitivity of our results to sedimentary (Fig. 2), resolution (Fig. S8), dimensionality reduction (Fig. S9, Fig. S10, Fig. S11, Fig. S12), power spectra and β estimation (Fig. S9, Fig. S10, Fig. S13, Fig. S14), and spatiotemporal sampling biases (Fig. S15, Fig. S16, Fig. S17) and find that our conclusions are insensitive to each (*28*).

We find that the spectral continuum of variability in vegetation turnover carries clear similarities to that of the climate system (Fig. 2), yet the relationship to climate varies with frequency. The power spectrum of vegetation turnover appears to follow the climate system across the scaling breakpoint reported in previous studies (*5*, *6*) and also found here, supporting the interpretation that vegetation dynamically tracks the climate system at intermediate frequencies (Fig. 1, Fig. 2, Table S1, 693^{-1}—649^{-1} $years^{-1}$ for temperature; 691^{-1}—660^{-1} $years^{-1}$ for precipitation; 862^{-1}—797^{-1} $years^{-1}$ for vegetation turnover) (*10*). However, unlike temperature and precipitation (*5*, *6*), the vegetation turnover power spectrum has two additional breakpoints, at 149^{-1} $years^{-1}$ (95% CI: 154^{-1}, 145^{-1}) and $18{,}012^{-1}$ $years^{-1}$ ($18{,}952^{-1}$, $17{,}254^{-1}$) (uncertainties for all parameters estimated are reported in Table S1). The vegetation turnover power spectra are therefore characterized by four scaling regimes: high frequencies (< 149^{-1} $years^{-1}$); high-intermediate frequencies (149^{-1} to 797^{-1} $years^{-1}$); low-intermediate frequencies (797^{-1} to $18{,}012^{-1}$ $years^{-1}$); and low frequencies (> $18{,}012^{-1}$ $years^{-1}$). The additional breakpoints in the continuum of the vegetation turnover power spectrum found in the global average (Fig. 2) are also found in the spectra of individual time series (Fig. S18), indicating that the patterns are not an artifact of the ensemble approach. Together, these features of the vegetation turnover power spectra provide evidence that the relationship between plant assemblages and climate is timescale-dependent and complex. Ecological communities and climate may co-vary on some timescales but differ in their dynamics on others, which we detail below.

Timescales of Ecological Dynamics

Coupled Dynamics

We show evidence of climate and vegetation coupling between 149^{-1} to $18{,}012^{-1}$ years^{-1} (Fig. 2), which is a narrower range of frequencies than previously theorized (*10*). First, for both vegetation and climate, βs are near zero at frequencies from 149^{-1} to 797^{-1} years^{-1}, and ~2 at frequencies from 797^{-1} to $18{,}012^{-1}$ years^{-1}. Second, scaling breakpoints are aligned for vegetation and climate between 672^{-1} and 797^{-1} years^{-1} (Fig. 1). This period of vegetation and climate coupling spans the theorized (*29*) and observed scaling break (*5*, *6*) that separates weather and climate variability and suggests a foundational shift in vegetation turnover from autocorrelated to stochastic at frequencies of ca. 670 to 800^{-1} years $^{-1}$ is related to coupled atmosphere-ocean-vegetation processes (*29*).

This finding sharpens our understanding of the frequencies at which plant communities rapidly and dynamically adjust composition and structure in response to climate forcing. Prior theory and the observations of orbital signals in pollen records have led to the widespread agreement of fast tracking of climate by vegetation composition at frequencies of $1{,}000^{-1}$ to $100{,}000^{-1}$ years^{-1} (*10*, *11*). However, whether vegetation rapidly tracks climate at sub-millennial frequencies (10^{-2} to 10^{-3} years^{-1}) was previously unclear, with evidence for and against climate disequilibrium at frequencies of 50^{-1} to 200^{-1} years^{-1} (*12*, *30*). Our work thus expands prior knowledge by suggesting climate tracking by vegetation for frequencies as short as 149^{-1} years^{-1}.

The small $\beta \sim 0$ for vegetation turnover between 149^{-1} to 797^{-1} years^{-1} indicates that variance is equally partitioned across this frequency range and suggests stochastic processes, such as extreme weather events or disturbances, yield small changes in abundance without a wholesale change in vegetation composition (Fig. 2). In contrast, a $\beta \sim 2$ from 797^{-1} to $18{,}012^{-1}$ years^{-1} indicates more variance at lower frequencies and autocorrelated dynamics. These dynamics can result from vegetation directly tracking autocorrelated processes in the climate system or from ecological processes that increase autocorrelation, such as density-dependent processes and priority effects.

Although the breakpoint for vegetation turnover at 797^{-1} years^{-1} is statistically distinguishable from temperature and precipitation (Table S2), these differences likely reflect the limitations of the approach. The non-random subset of communities recorded by these vegetation assemblage records, our choice of climate model, or biased local/regional spectral estimates from climate models (*31*) all could affect the precise location of the breakpoint and lead to an apparent offset. However, if this offset between the vegetation and climate breakpoints is real, two hypotheses may explain the brief decoupling of climate and vegetation between frequencies of 676^{-1}—672^{-1} years^{-1} and 797^{-1} years^{-1}: a lag in vegetation response to the transition from low β to higher β weather-climate scaling regimes or the greater importance of non-climatic forcing (such as disturbance regimes) at these frequencies.

Uncoupled Dynamics

Vegetation and climate appear decoupled at frequencies higher than 149^{-1} years^{-1} and lower than $18{,}012^{-1}$ years^{-1}. β is 4.34 (3.64, 4.96) for vegetation turnover at the highest frequencies, while for temperature and precipitation, β is -0.24 (-0.29, -0.18) and -0.52 (-0.58, -0.49), respectively (Fig. 2, Table S1). This finding supports prior observations of higher βs in vegetation turnover at

these high frequencies (*32*) but appears sensitive to the amount of weight given to abundant and rare taxa when estimating vegetation turnover with dissimilarity metrics and the fossil pollen record under consideration (Fig. S9). Some combination of taphonomy, sampling, and ecological processes could explain higher βs in vegetation turnover at these high frequencies. Decadal-scale mixing of lake sediments and scale gaps caused by discontinuous sampling of sediments may enhance autocorrelation in vegetation turnover variability from these archives (*33*, *34*). In addition, the large βs at the highest frequencies may result from the long life spans of some plants (e.g. trees, which are well-represented in fossil pollen assemblages), limiting the ability of the full assemblage to track high frequency climate variability due to slow turnover times. Indeed, the median tree lifespan from the International Tree Ring Data Bank (*35*, *36*) is 246 years (n = 4,773) (Fig. S19). A long lifespan may impart a high β as vegetation turnover would increase approaching the frequency of median tree longevity from increasing mortality. Anthropogenic land use change may also contribute to climate decoupling at high frequencies (*37*, *38*), possibly interacting with tree longevity. Notably, a greater β for vegetation turnover at the highest frequencies is consistent with observations of slow vegetation responses to climate variability and evidence of climate debt (*13–15*, *39*). These slow responses are expected to create mismatches between species' climate preferences and climate and thus reduce organismal fitness and ecosystem function.

For frequencies lower than $18{,}012^{-1}$ years^{-1} ($18{,}952^{-1}$, $17{,}254^{-1}$), β=-0.08 (-0.23, -0.06) for the vegetation turnover power spectrum (Fig. 2). This contrasts with the climate power spectra, which maintain the long-term climate system βs of ~2-3 due to the influence of astronomical forcing (Fig. 2) (*40*). There are two possible explanations for low βs in vegetation turnover at these low frequencies. First, the community dissimilarity metric we use to quantify vegetation turnover within each time series may reach a maximum value (i.e. metric saturation, Fig. S20) and fail to record turnover beyond a complete replacement of the vegetation assemblage (*41*). For example, if climate change caused multiple assemblage turnovers (assemblage A replaced by B replaced by C), community dissimilarity metrics will saturate and underestimate the true ecological impact of past climate change, producing an apparent decrease in vegetation turnover with decreasing frequency. Second, fast evolutionary adaptation would increase species tolerance to environmental variation and result in vegetation communities appearing relatively resistant to climate forcing. Although local adaptation cannot be excluded as an explanation, the hypothesis of metric saturation appears sufficient to explain the reduced vegetation turnover variability at low frequencies (Fig. S9).

Non-Linearity in the Climate-Vegetation Relationship

High spectral power at $4{,}650^{-1}$ years^{-1} is unique to vegetation turnover and is absent in the power spectra of the climate proxies and climate simulations we evaluated (Fig. 2, Fig. S3). Climate in the North Atlantic has been argued to contain apparent modes of climate variability at $1{,}470^{-1}$ and $4{,}670^{-1}$ years^{-1} (*42*) and provides a plausible mechanism for forcing vegetation turnover (*30*, *43*, *44*). However, global compilations of Holocene climate records lack high spectral power at any of these frequencies (Fig. S3)(*45*), as do the spectra of simulated temperature and precipitation (Fig. 2). This disconnect at the global scale (and in the subset of sites we investigated) between climate and vegetation turnover leads us to hypothesize that relatively

subtle or regional millennial-scale climate variations are amplified in the vegetation response by non-linear ecological dynamics (*27*, *46*).

However, analytical artifacts may also contribute to high spectral power at $4{,}650^{-1}$ years^{-1}. Most of our records span 20,000 years, with fewer longer records (186 sites, Fig. S1, Data S1). The relatively low number of sites sampled could bias our spatial and environmental coverage at low frequencies, producing a spurious peak in spectral power. Despite these potential artifacts, evidence for nonlinear responses in vegetation assemblages to small environmental changes is well-documented (*27*). Our observations suggest slow vegetation responses to climate variability at high frequencies alongside high turnover at $4{,}650^{-1}$ years^{-1}, demonstrating how gradual vegetation changes can be accompanied by abrupt, nonlinear shifts in vegetation assemblages. Hence, even without clear patterns of climate variability in the North Atlantic at this frequency, the vegetation dynamics over the last 600,000 years underscore the potential for abrupt changes in plant assemblages over the coming decades of warming (*47*).

Latitudinal Gradient in Assemblage Dynamics

We find that the relationship between vegetation turnover variability and climate variability differs across latitudes. Climatically, the high latitudes experience greater temperature variability than the tropics at all frequencies (*5*), while the tropics experience greater precipitation variability (Fig. 3). Even though accurately simulating precipitation remains challenging, vegetation turnover appears to resemble temperature, in that tropical sites ($< 23.5°$) have less vegetation variability than extra-tropical sites ($> 23.5°$) (Fig. 3A). In addition, at frequencies of 712^{-1} (730^{-1}, 698^{-1}) to $13{,}885^{-1}$ ($14{,}495^{-1}$, $13{,}160^{-1}$) years^{-1}, extra-tropical sites have a β of 2.20 (2.16, 2.26) that is similar to those of temperature and precipitation, while tropical sites have a β of 1.30 (1.21, 1.38) (Fig. 3). Thus, tropical vegetation assemblages may be less sensitive to climate forcing across the frequencies investigated, are sensitive to climate forcings other than temperature and precipitation, are affected more by non-climatic factors, or are more stable and resistant to turnover. Along these lines, recent observations show that while net primary production in low latitudes is constrained by solar radiation and precipitation, high northern latitude productivity is limited by temperature (*48*), suggesting these latitudinal differences in β could result from spatially variable climate controls on vegetation variability.

Conclusions

Our theoretical framework, based on spectral analyses, provides a new pathway forward to disentangle a fundamental question in ecology: how closely are ecological dynamics coupled or decoupled with environmental dynamics across timescales? The methods shown here are flexible and adaptable to all ecological systems with observational data across a range of timescales. Through this framework, we show that the relationship between vegetation turnover and climate variability is non-linear and timescale-dependent over frequencies from 10^{-1} to $100{,}000^{-1}$ years^{-1}. The many similarities between vegetation and climate power spectra suggest that vegetation variation is governed by climate variability across intermediate frequencies. Modes of heightened variability in vegetation relative to climate at millennial frequencies underscore the risk of nonlinear and abrupt vegetation responses to current climate change. Conversely, the decoupling of vegetation and climate variability at higher frequencies ($>149^{-1}$ years^{-1}) reinforces

concerns that biotic processes will be slow to respond to anthropogenic climate change and changing climate variability (*12*, *49*), leading to delayed and widespread ecological transitions that challenge predicting vegetation responses to current warming.

Acknowledgements

We are grateful to Yasuhiro Kubota for convening the P-SEEDS workshop where the idea for this project began. Many thanks to the Syracuse University High Throughput Computing Campus Grid (OrangeGrid) for providing computational resources and to Jon Cheney for technical support. Fossil pollen data were obtained from the Neotoma Paleoecology Database (http://www.neotomadb.org) and its constituent databases: the African Pollen Database, European Pollen Database, Indo-Pacific Pollen Database, Latin American Pollen Database, and North American Pollen Database. The work of data contributors, data stewards, and the Neotoma community is gratefully acknowledged. We thank the anonymous reviewers for their feedback, which greatly improved the manuscript. **Funding:** This project is a contribution to the BioDeepTime project, supported by Paleosynthesis Project, which is funded by the Volkswagen Foundation (Az 96 796). DF acknowledges postdoctoral support from NSF OCE-2103015, NSF AGS-2402498, and the College of Arts and Sciences at Syracuse University. Funding for OrangeGrid is provided by ACI-1341006. EES acknowledges support from a Leverhulme Prize and NERC grant NE/V011405/1. LJ is supported through the German climate modeling initiative PALMOD, funded by the German Ministry of Science and Education (BMBF, 01LP1922A). MCR acknowledges support from the German Research Foundation (DFG) through the Cluster of Excellence 'The Ocean Floor – Earth's Uncharted Interface' (EXC 2077, grant no. 390741603). PMH acknowledges sabbatical support from the Swiss Federal Institute for Forest, Snow and Landscape Research. SRM acknowledges sabbatical support from UW-Madison and a Guggenheim Fellowship. JWW acknowledges sabbatical support from UW-Madison and NSF award 2410961. **Author contributions:** DF and PMH developed the research questions and study design. DF, SRM, EES, JWW, and PMH co-developed the conceptual and analytical framework. DF performed all analyses with help from SRM and EES. DF led writing with support from SRM, EES, JWW, and PMH. The ideas for this paper originated from discussions in the BioDeepTime working group. All authors reviewed and contributed to the article. **Data and materials availability:** Data and code needed to reproduce all analyses are available on Zenodo (74).

Figures

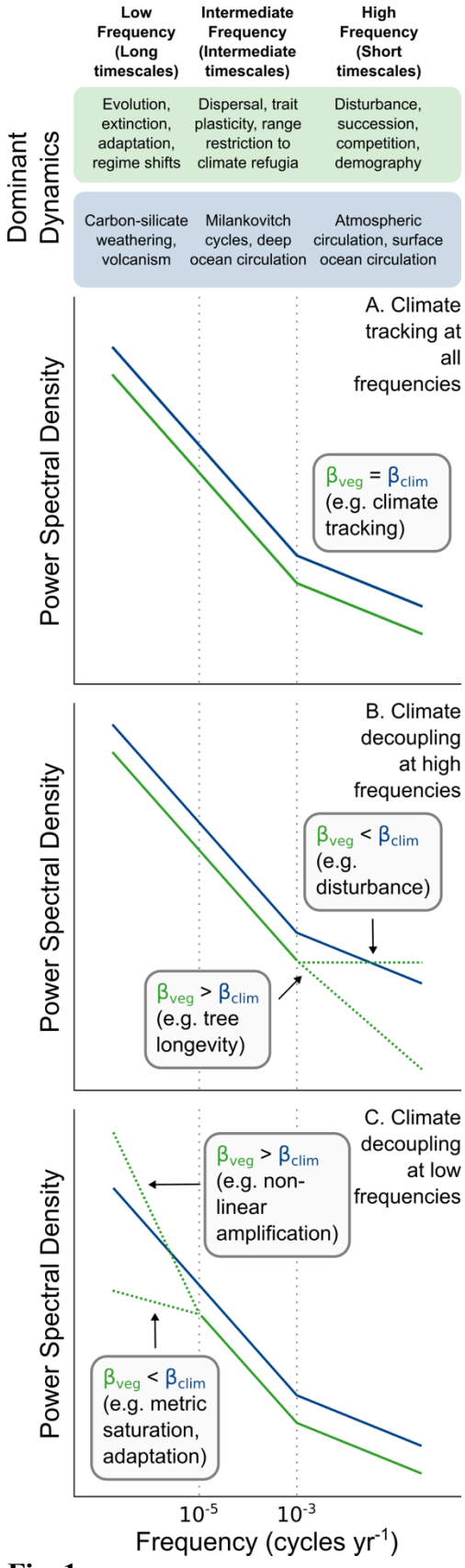
Low Frequency (Long timescales)
Intermediate Frequency (Intermediate timescales)
High Frequency (Short timescales)
Dominant Dynamics
Evolution, extinction, adaptation, regime shifts
Dispersal, trait plasticity, range restriction to climate refugia
Disturbance, succession, competition, demography
Carbon-silicate weathering, volcanism
Milankovitch cycles, deep ocean circulation
Atmospheric circulation, surface ocean circulation
A. Climate tracking at all frequencies
Power Spectral Density
βveg = βclim (e.g. climate tracking)
B. Climate decoupling at high frequencies
βveg < βclim (e.g. disturbance)
βveg > βclim (e.g. tree longevity)
C. Climate decoupling at low frequencies
βveg > βclim (e.g. non-linear amplification)
βveg < βclim (e.g. metric saturation, adaptation)
10-5
10-3
Frequency (cycles yr-1)

Fig. 1

Conceptual framework for eco-climate spectral analyses

A conceptual framework for interpreting the relationship between vegetation and climate using power spectra through the power-law scaling relationship between spectral power and frequency ($S(f) \propto f^{-\beta}$). The blue line corresponds to β for climate variability and the green line corresponds to β for vegetation compositional turnover. The breakpoint in climate spectral power in all three panels is based on prior work that indicates a breakpoint in climate variability at approximately 100^{-1} to $1{,}000^{-1}$ $years^{-1}$ (*5*, *6*). Key characteristics include the slope (β, i.e. continuum) of vegetation turnover relative to climate and the placement of breakpoints (dashed vertical lines). Three scenarios illustrate potential relationships between climate and vegetation. (A) Vegetation composition exhibits linear responses to climate across all frequencies and so the slope of vegetation spectral power parallels that of climate (*10*). (B) Vegetation linearly tracks climate at intermediate frequencies and low frequencies (*10*) but is decoupled from climate at high frequencies (*50*). At high frequencies, a higher β for vegetation than climate suggests that processes such as tree longevity influence vegetation turnover while a lower β for vegetation indicates that disturbance may be a primary control on turnover (*25*). (C) Vegetation tracks climate across high and intermediate frequencies but is decoupled at low frequencies from processes like evolutionary adaptation (lower β for vegetation) or non-linear amplification through processes such as threshold responses (higher β for vegetation). Other scenarios and biological processes are possible beyond those shown here.

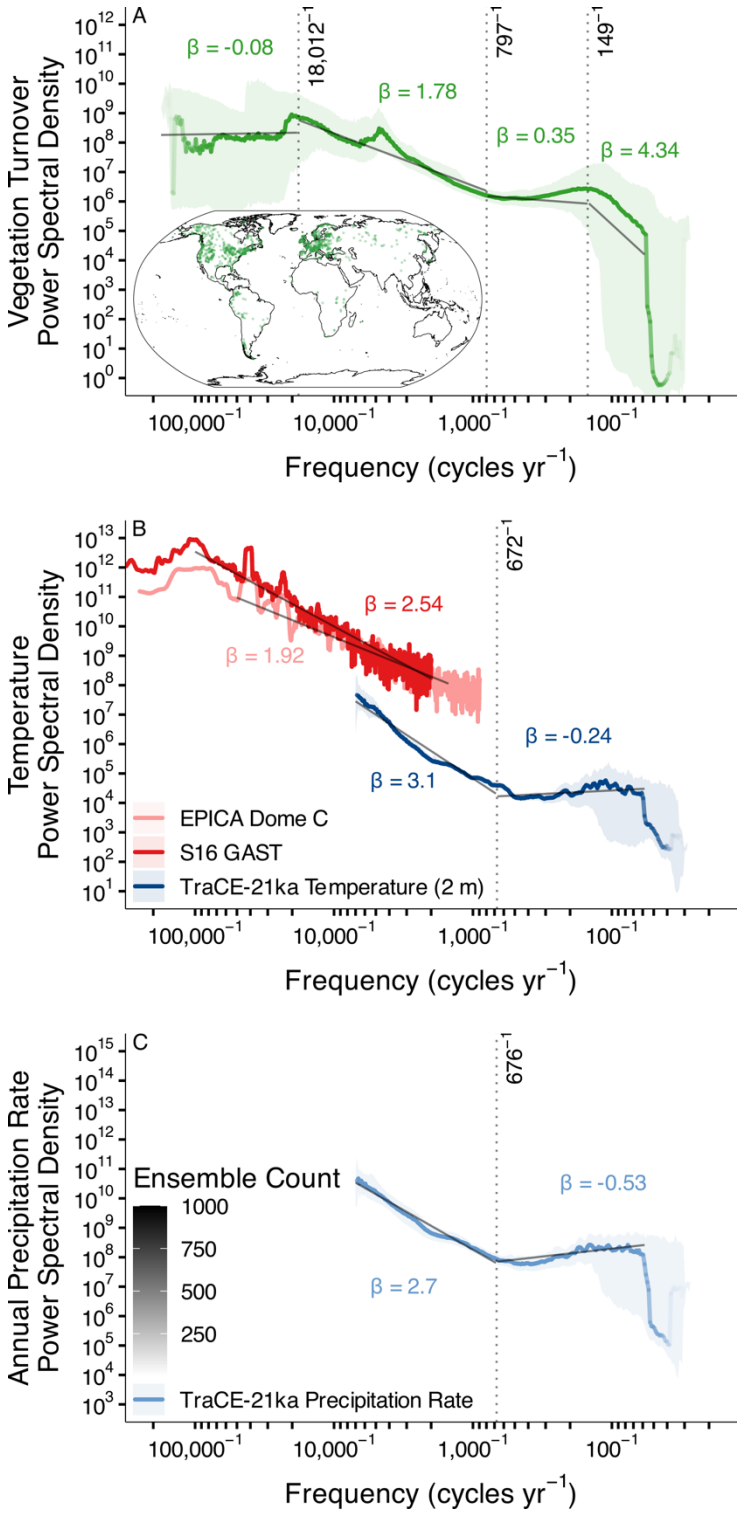

Fig. 2

The continuum of global vegetation turnover and climate variability

The spectral continuum of (A) vegetation turnover (green), (B) temperature (blue, red, pink), and (C) precipitation (light blue) variability based on the median from an ensemble of spectral power estimates. Power spectra line opacity indicates the number of ensemble members that resolve each frequency with the corresponding legend for all plots in (C). β in the high frequency band

was fit to the maximum frequency that yielded an unbiased estimate (*28*). Solid gray lines correspond to β from ordinary least squares regressions of log-spectral power and log-frequency. Vertical dashed lines correspond to breakpoints identified in the spectral continuum. Climate estimates from TraCE-21ka have been downsampled in space and time and low-pass filtered to match the temporal characteristics of the fossil pollen abundances. Uncertainties for β and breakpoints and permutation tests comparing these parameters are reported in Table S1, Table S3 - Table S2, Fig. S21.

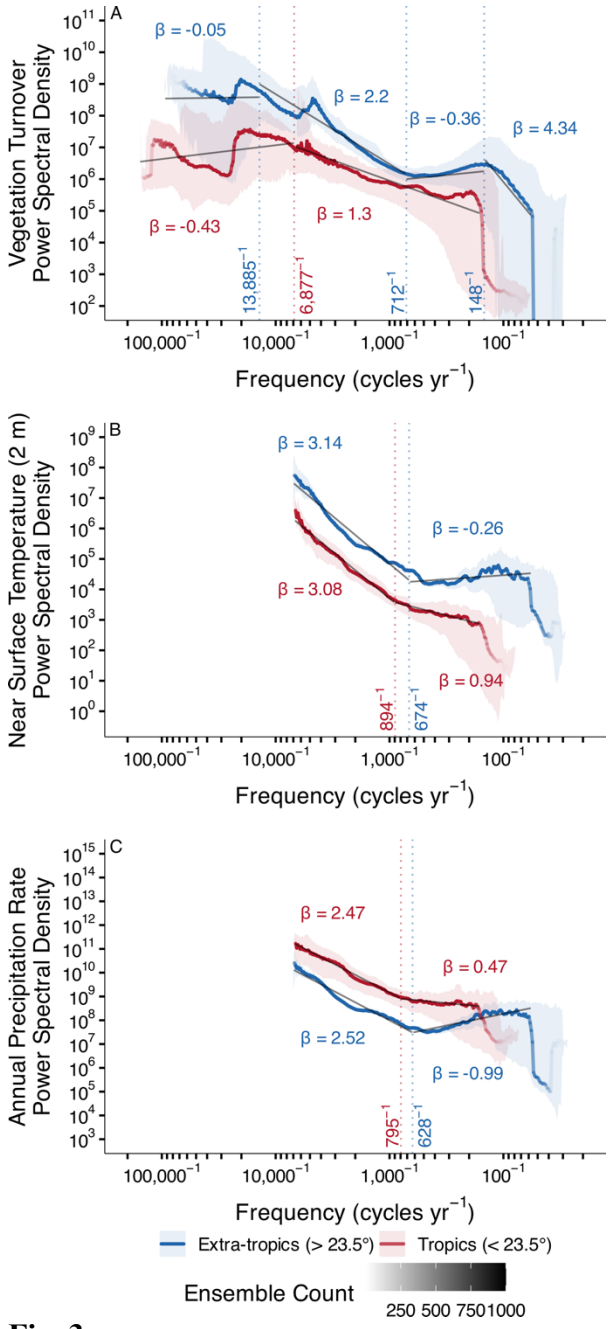

Fig. 3

The continuum of tropical and extra-tropical vegetation turnover and climate variability

The continuum of (A) vegetation turnover, (B) near-surface temperature, and (C) annual precipitation rate variability, averaged for the extra-tropics (blue, > 23.5°) and tropics (red, < 23.5°) based on the median from an ensemble of spectral power estimates. Power spectra line opacity indicates the number of ensemble members that resolve each frequency. β in the high frequency band was fit to the maximum frequency that yielded an unbiased estimate (*28*). Vertical dashed lines correspond to breakpoints identified in the spectral continuum and are colored by the corresponding spatial average. All climate estimates are from TraCE-21ka and have been downsampled as in Fig. 2. Uncertainties for β and breakpoints, and permutation tests comparing these parameters, are reported in Table S1, Table S4 - Table S7, Fig. S22.

References

1. J. Overpeck, C. Whitlock, B. Huntley, "Terrestrial Biosphere Dynamics in the Climate System: Past and Future" in *Paleoclimate, Global Change and the Future*, K. D. Alverson, T. F. Pedersen, R. S. Bradley, Eds. (Springer, Berlin, Heidelberg, 2003; https://doi.org/10.1007/978-3-642-55828-3_5)*Global Change — The IGBP Series*, pp. 81–103.

2. E. M. Wolkovich, B. I. Cook, K. K. McLauchlan, T. J. Davies, Temporal ecology in the Anthropocene. *Ecology Letters* **17**, 1365–1379 (2014).

3. D. Jablonski, Biotic interactions and macroevolution: extensions and mismatches across scales and levels. *Evolution* **62**, 715–739 (2008).

4. R. E. Ricklefs, Community Diversity: Relative Roles of Local and Regional Processes. *Science* **235**, 167–171 (1987).

5. P. Huybers, W. Curry, Links between annual, Milankovitch and continuum temperature variability. *Nature* **441**, 329–332 (2006).

6. F. Zhu, J. Emile-Geay, N. P. McKay, G. J. Hakim, D. Khider, T. R. Ault, E. J. Steig, S. Dee, J. W. Kirchner, Climate models can correctly simulate the continuum of global-average temperature variability. *Proceedings of the National Academy of Sciences* **116**, 8728–8733 (2019).

7. M. Yasuhara, R. Danovaro, Temperature impacts on deep-sea biodiversity. *Biological Reviews* **91**, 275–287 (2016).

8. J. W. Williams, E. C. Grimm, J. L. Blois, D. F. Charles, E. B. Davis, S. J. Goring, R. W. Graham, A. J. Smith, M. Anderson, J. Arroyo-Cabrales, A. C. Ashworth, J. L. Betancourt, B. W. Bills, R. K. Booth, P. I. Buckland, B. B. Curry, T. Giesecke, S. T. Jackson, C. Latorre, J. Nichols, T. Purdum, R. E. Roth, M. Stryker, H. Takahara, The Neotoma Paleoecology Database, a multiproxy, international, community-curated data resource. *Quaternary Research* **89**, 156–177 (2018).

9. J. Smith, M. C. Rillo, Á. T. Kocsis, M. Dornelas, D. Fastovich, H.-H. M. Huang, L. Jonkers, W. Kiessling, Q. Li, L. H. Liow, M. Margulis-Ohnuma, S. Meyers, L. Na, A. M. Penny, K. Pippenger, J. Renaudie, E. E. Saupe, M. J. Steinbauer, M. Sugawara, A. Tomašovỳch, J. W. Williams, M. Yasuhara, S. Finnegan, P. M. Hull, BioDeepTime: A database of biodiversity time series for modern and fossil assemblages. *Global Ecology and Biogeography* **n/a** (2023).

10. T. Webb, Is vegetation in equilibrium with climate? How to interpret late-Quaternary pollen data. *Vegetatio* **67**, 75–91 (1986).

11. J. W. Williams, A. Ordonez, J.-C. Svenning, A unifying framework for studying and managing climate-driven rates of ecological change. *Nat Ecol Evol* **5**, 17–26 (2021).

12. J.-C. Svenning, B. Sandel, Disequilibrium vegetation dynamics under future climate change. *American Journal of Botany* **100**, 1266–1286 (2013).

13. M. V. Talluto, I. Boulangeat, S. Vissault, W. Thuiller, D. Gravel, Extinction debt and colonization credit delay range shifts of eastern North American trees. *Nat Ecol Evol* **1**, 1–6 (2017).

14. R. Bertrand, J. Lenoir, C. Piedallu, G. Riofrío-Dillon, P. de Ruffray, C. Vidal, J.-C. Pierrat, J.-C. Gégout, Changes in plant community composition lag behind climate warming in lowland forests. *Nature* **479**, 517–520 (2011).

15. B. J. Butterfield, R. S. Anderson, C. A. Holmgren, J. L. Betancourt, Extinction debt and delayed colonization have had comparable but unique effects on plant community–climate lags since the Last Glacial Maximum. *Global Ecology and Biogeography* **28**, 1067–1077 (2019).

16. M. Scheffer, S. Carpenter, J. A. Foley, C. Folke, B. Walker, Catastrophic shifts in ecosystems. *Nature* **413**, 591–596 (2001).

17. D. J. Thomson, Spectrum estimation and harmonic analysis. *Proceedings of the IEEE* **70**, 1055–1096 (1982).

18. F. He, *Simulating Transient Climate Evolution of the Last Deglaciation with CCSM 3* (2011)vol. 72.

19. Z. Liu, B. L. Otto-Bliesner, F. He, E. C. Brady, R. Tomas, P. U. Clark, A. E. Carlson, J. Lynch-Stieglitz, W. Curry, E. Brook, D. Erickson, R. Jacob, J. Kutzbach, J. Cheng, Transient Simulation of Last Deglaciation with a New Mechanism for Bølling-Allerød Warming. *Science* **325**, 310–314 (2009).

20. C. W. Snyder, Evolution of global temperature over the past two million years. *Nature* **538**, 226–228 (2016).

21. J. Jouzel, V. Masson-Delmotte, O. Cattani, G. Dreyfus, S. Falourd, G. Hoffmann, B. Minster, J. Nouet, J. M. Barnola, J. Chappellaz, H. Fischer, J. C. Gallet, S. Johnsen, M. Leuenberger, L. Loulergue, D. Luethi, H. Oerter, F. Parrenin, G. Raisbeck, D. Raynaud, A. Schilt, J. Schwander, E. Selmo, R. Souchez, R. Spahni, B. Stauffer, J. P. Steffensen, B. Stenni, T. F. Stocker, J. L. Tison, M. Werner, E. W. Wolff, Orbital and Millennial Antarctic Climate Variability over the Past 800,000 Years. *Science* **317**, 793–796 (2007).

22. T. Platt, K. L. Denman, Spectral Analysis in Ecology. *Annu. Rev. Ecol. Syst.* **6**, 189–210 (1975).

23. M. E. Dillon, H. A. Woods, G. Wang, S. B. Fey, D. A. Vasseur, R. S. Telemeco, K. Marshall, S. Pincebourde, Life in the Frequency Domain: the Biological Impacts of Changes in Climate Variability at Multiple Time Scales. *Integrative and Comparative Biology* **56**, 14–30 (2016).

24. G. M. Locosselli, R. J. W. Brienen, M. de S. Leite, M. Gloor, S. Krottenthaler, A. A. de Oliveira, J. Barichivich, D. Anhuf, G. Ceccantini, J. Schöngart, M. Buckeridge, Global tree-ring analysis reveals rapid decrease in tropical tree longevity with temperature. *Proceedings of the National Academy of Sciences* **117**, 33358–33364 (2020).

25. L. B. Brubaker, Responses of tree populations to climatic change. *Vegetatio* **67**, 119–130 (1986).

26. R. Rauschkolb, Z. Li, S. Godefroid, L. Dixon, W. Durka, M. Májeková, O. Bossdorf, A. Ensslin, J. F. Scheepens, Evolution of plant drought strategies and herbivore tolerance after two decades of climate change. *New Phytologist* **235**, 773–785 (2022).

27. J. W. Williams, J. L. Blois, B. N. Shuman, Extrinsic and intrinsic forcing of abrupt ecological change: case studies from the late Quaternary. *Journal of Ecology* **99**, 664–677 (2011).

28. Materials and methods are available as supplementary materials.

29. K. Hasselmann, Stochastic climate models Part I. Theory. *Tellus* **28**, 473–485 (1976).

30. J. W. Williams, D. M. Post, L. C. Cwynar, A. F. Lotter, A. J. Levesque, Rapid and widespread vegetation responses to past climate change in the North Atlantic region. *Geology* **30**, 971–974 (2002).

31. T. Laepple, E. Ziegler, N. Weitzel, R. Hébert, B. Ellerhoff, P. Schoch, B. Martrat, O. Bothe, E. Moreno-Chamarro, M. Chevalier, A. Herbert, K. Rehfeld, Regional but not global temperature variability underestimated by climate models at supradecadal timescales. *Nat. Geosci.* **16**, 958–966 (2023).

32. R. Hébert, L. Schild, T. Laepple, U. Herzschuh, Biome- and timescale-dependence of Holocene vegetation variability in the Northern Hemisphere. *Ecology and Evolution* **13**, e10585 (2023).

33. R. Hébert, K. Rehfeld, T. Laepple, Comparing estimation techniques for temporal scaling in palaeoclimate time series. *Nonlinear Processes in Geophysics* **28**, 311–328 (2021).

34. R. B. Davis, Stratigraphic effects of tubificids in profundal lake sediments. *Limnology and Oceanography* **19**, 466–488 (1974).

35. H. D. Grissino-Mayer, H. C. Fritts, The International Tree-Ring Data Bank: an enhanced global database serving the global scientific community. *The Holocene* **7**, 235–238 (1997).

36. S. Zhao, N. Pederson, L. D'Orangeville, J. HilleRisLambers, E. Boose, C. Penone, B. Bauer, Y. Jiang, R. D. Manzanedo, The International Tree-Ring Data Bank (ITRDB) revisited: Data availability and global ecological representativity. *Journal of Biogeography* **46**, 355–368 (2019).

37. O. Mottl, S. G. A. Flantua, K. P. Bhatta, V. A. Felde, T. Giesecke, S. Goring, E. C. Grimm, S. Haberle, H. Hooghiemstra, S. Ivory, P. Kuneš, S. Wolters, A. W. R. Seddon, J. W. Williams, Global acceleration in rates of vegetation change over the past 18,000 years. *Science* **372**, 860–864 (2021).

38. L. Stephens, D. Fuller, N. Boivin, T. Rick, N. Gauthier, A. Kay, B. Marwick, C. G. Armstrong, C. M. Barton, T. Denham, K. Douglass, J. Driver, L. Janz, P. Roberts, J. D. Rogers, H. Thakar, M. Altaweel, A. L. Johnson, M. M. Sampietro Vattuone, M. Aldenderfer, S. Archila, G. Artioli, M. T. Bale, T. Beach, F. Borrell, T. Braje, P. I. Buckland, N. G. Jiménez Cano, J. M. Capriles, A. Diez Castillo, Ç. Çilingiroğlu, M. Negus Cleary, J. Conolly, P. R. Coutros, R. A. Covey, M. Cremaschi, A. Crowther, L. Der, S. di Lernia, J. F. Doershuk, W. E. Doolittle, K. J. Edwards, J. M. Erlandson, D. Evans, A. Fairbairn, P. Faulkner, G. Feinman, R. Fernandes, S. M. Fitzpatrick, R. Fyfe, E. Garcea, S. Goldstein, R. C. Goodman, J. Dalpoim Guedes, J. Herrmann, P. Hiscock, P. Hommel, K. A. Horsburgh, C. Hritz, J. W. Ives, A. Junno, J. G. Kahn, B. Kaufman, C. Kearns, T. R. Kidder, F.

Lanoë, D. Lawrence, G.-A. Lee, M. J. Levin, H. B. Lindskoug, J. A. López-Sáez, S. Macrae, R. Marchant, J. M. Marston, S. McClure, M. D. McCoy, A. V. Miller, M. Morrison, G. Motuzaite Matuzeviciute, J. Müller, A. Nayak, S. Noerwidi, T. M. Peres, C. E. Peterson, L. Proctor, A. R. Randall, S. Renette, G. Robbins Schug, K. Ryzewski, R. Saini, V. Scheinsohn, P. Schmidt, P. Sebillaud, O. Seitsonen, I. A. Simpson, A. Sołtysiak, R. J. Speakman, R. N. Spengler, M. L. Steffen, M. J. Storozum, K. M. Strickland, J. Thompson, T. L. Thurston, S. Ulm, M. C. Ustunkaya, M. H. Welker, C. West, P. R. Williams, D. K. Wright, N. Wright, M. Zahir, A. Zerboni, E. Beaudoin, S. Munevar Garcia, J. Powell, A. Thornton, J. O. Kaplan, M.-J. Gaillard, K. Klein Goldewijk, E. Ellis, Archaeological assessment reveals Earth's early transformation through land use. *Science* **365**, 897–902 (2019).

39. K. Zhu, C. W. Woodall, J. S. Clark, Failure to migrate: lack of tree range expansion in response to climate change. *Global Change Biology* **18**, 1042–1052 (2012).

40. S. R. Meyers, L. A. Hinnov, Northern Hemisphere glaciation and the evolution of Plio-Pleistocene climate noise. *Paleoceanography* **25** (2010).

41. S. Ferrier, G. Manion, J. Elith, K. Richardson, Using generalized dissimilarity modelling to analyse and predict patterns of beta diversity in regional biodiversity assessment. *Diversity and Distributions* **13**, 252–264 (2007).

42. G. Bond, W. Showers, M. Cheseby, R. Lotti, P. Almasi, P. deMenocal, P. Priore, H. Cullen, I. Hajdas, G. Bonani, A pervasive millennial-scale cycle in North Atlantic Holocene and glacial climates. *Science* **278**, 1257–1266 (1997).

43. D. Fastovich, J. M. Russell, S. T. Jackson, T. R. Krause, S. A. Marcott, J. W. Williams, Spatial fingerprint of Younger Dryas cooling and warming in eastern North America. *Geophysical Research Letters* **47**, e2020GL090031 (2020).

44. B. Huntley, J. R. M. Allen, Y. C. Collingham, T. Hickler, A. M. Lister, J. Singarayer, A. J. Stuart, M. T. Sykes, P. J. Valdes, Millennial climatic fluctuations are key to the structure of last glacial ecosystems. *PloS one* **8** (2013).

45. H. Wanner, J. Beer, J. Butikofer, T. J. Crowley, U. Cubasch, J. Fluckiger, H. Goosse, M. Grosjean, F. Joos, J. O. Kaplan, M. Kuttel, S. A. Muller, I. C. Prentice, O. Solomina, T. F. Stocker, P. Tarasov, M. Wagner, M. Widmann, Mid- to Late Holocene climate change: an overview. *Quaternary Science Reviews* **27**, 1791–1828 (2008).

46. D. Magri, Patterns of post-glacial spread and the extent of glacial refugia of European beech (Fagus sylvatica). *Journal of Biogeography* **35**, 450–463 (2008).

47. M. G. Turner, W. J. Calder, G. S. Cumming, T. P. Hughes, A. Jentsch, S. L. LaDeau, T. M. Lenton, B. N. Shuman, M. R. Turetsky, Z. Ratajczak, J. W. Williams, A. P. Williams, S. R. Carpenter, Climate change, ecosystems and abrupt change: science priorities. *Philosophical Transactions of the Royal Society B: Biological Sciences* **375**, 20190105 (2020).

48. R. R. Nemani, C. D. Keeling, H. Hashimoto, W. M. Jolly, S. C. Piper, C. J. Tucker, R. B. Myneni, S. W. Running, Climate-Driven Increases in Global Terrestrial Net Primary Production from 1982 to 1999. *Science* **300**, 1560–1563 (2003).

49. J. Aguirre-Gutiérrez, S. Díaz, S. W. Rifai, J. J. Corral-Rivas, M. G. Nava-Miranda, R. González-M, A. B. Hurtado-M, N. S. Revilla, E. Vilanova, E. Almeida, E. A. de Oliveira, E. Alvarez-Davila, L. F. Alves, A. C. S. de Andrade, A. C. Lola da Costa, S. A. Vieira, L. Aragão, E. Arets, G. A. Aymard C., F. Baccaro, Y. V. Bakker, T. R. Baker, O. Bánki, C. Baraloto, P. B. de Camargo, E. Berenguer, L. Blanc, D. Bonal, F. Bongers, K. M. Bordin, R. Brienen, F. Brown, N. C. C. S. Prestes, C. V. Castilho, S. C. Ribeiro, F. C. de Souza, J. A. Comiskey, F. C. Valverde, S. C. Müller, R. da Costa Silva, J. D. do Vale, V. de Andrade Kamimura, R. de Oliveira Perdiz, J. del Aguila Pasquel, G. Derroire, A. Di Fiore, M. Disney, W. Farfan-Rios, S. Fauset, T. R. Feldpausch, R. F. Ramos, G. F. Llampazo, V. F. Martins, C. Fortunel, K. G. Cabrera, J. G. Barroso, B. Hérault, R. Herrera, E. N. Honorio Coronado, I. Huamantupa-Chuquimaco, J. J. Pipoly, K. J. Zanini, E. Jiménez, C. A. Joly, M. Kalamandeen, J. Klipel, A. Levesley, W. L. Oviedo, W. E. Magnusson, R. M. dos Santos, B. S. Marimon, B. H. Marimon-Junior, S. M. de Almeida Reis, O. A. Melo Cruz, A. M. Mendoza, P. Morandi, R. Muscarella, H. Nascimento, D. A. Neill, I. O. Menor, W. A. Palacios, S. Palacios-Ramos, N. C. Pallqui Camacho, G. Pardo, R. T. Pennington, L. de Oliveira Pereira, G. Pickavance, R. C. Picolotto, N. C. A. Pitman, A. Prieto, C. Quesada, H. Ramírez-Angulo, M. Réjou-Méchain, Z. R. Correa, J. M. Reyna Huaymacari, C. R. Rodriguez, G. Rivas-Torres, A. Roopsind, A. Rudas, B. Salgado Negret, M. T. van der Sande, F. D. Santana, F. A. Maës Santos, R. S. Bergamin, M. R. Silman, C. Silva, J. S. Espejo, M. Silveira, F. C. Souza, M. J. P. Sullivan, V. Swamy, J. Talbot, J. J. Terborgh, P. J. van der Meer, G. van der Heijden, B. van Ulft, R. V. Martinez, L. Vedovato, J. Vleminckx, V. A. Vos, V. Wortel, P. A. Zuidema, J. A. Zwerts, S. G. W. Laurance, W. F. Laurance, J. Chave, J. W. Dalling, J. Barlow, L. Poorter, B. J. Enquist, H. ter Steege, O. L. Phillips, D. Galbraith, Y. Malhi, Tropical forests in the Americas are changing too slowly to track climate change. *Science* **387**, eadl5414 (2025).

50. M. B. Davis, "Quaternary history and the stability of forest communities" in *Forest Succession: Concepts and Application*, D. C. West, H. H. Shugart, D. B. Botkin, Eds. (Springer New York, New York, NY, 1981; https://doi.org/10.1007/978-1-4612-5950-3_10), pp. 132–153.

51. M. Chevalier, B. A. S. Davis, O. Heiri, H. Seppa, B. M. Chase, K. Gajewski, T. Lacourse, R. J. Telford, W. Finsinger, J. Guiot, N. Kuhl, S. Y. Maezumi, J. R. Tipton, V. A. Carter, T. Brussel, L. N. Phelps, A. Dawson, M. Zanon, F. Valle, C. Nolan, A. Mauri, A. de Vernal, K. Izumi, L. Holmstrom, J. Marsicek, S. Goring, P. S. Sommer, M. Chaput, D. Kupriyanov, Pollen-based climate reconstruction techniques for late Quaternary studies. *Earth-Sci. Rev.* **210**, 33 (2020).

52. T. Webb, S. E. Howe, R. H. W. Bradshaw, K. M. Heide, Estimating plant abundances from pollen percentages: The use of regression analysis. *Review of Palaeobotany and Palynology* **34**, 269–300 (1981).

53. A. Parnell, Bchron: Radiocarbon dating, age-depth modelling, relative sea level rate estimation, and non-parametric phase modelling. *R package version* **4** (2014).

54. A. C. Parnell, J. Sweeney, T. K. Doan, M. Salter-Townshend, J. R. M. Allen, B. Huntley, J. Haslett, Bayesian inference for palaeoclimate with time uncertainty and stochastic volatility, *Journal of the Royal Statistical Society: Series C (Applied Statistics)*. **64** (2014)pp. 115–138.

55. P. J. Reimer, W. E. N. Austin, E. Bard, A. Bayliss, P. G. Blackwell, C. B. Ramsey, M. Butzin, H. Cheng, R. L. Edwards, M. Friedrich, P. M. Grootes, T. P. Guilderson, I. Hajdas, T. J. Heaton, A. G. Hogg, K. A. Hughen, B. Kromer, S. W. Manning, R. Muscheler, J. G. Palmer, C. Pearson, J. van der Plicht, R. W. Reimer, D. A. Richards, E. M. Scott, J. R. Southon, C. S. M. Turney, L. Wacker, F. Adolphi, U. Büntgen, M. Capano, S. M. Fahrni, A. Fogtmann-Schulz, R. Friedrich, P. Köhler, S. Kudsk, F. Miyake, J. Olsen, F. Reinig, M. Sakamoto, A. Sookdeo, S. Talamo, The IntCal20

Northern Hemisphere Radiocarbon Age Calibration Curve (0–55 cal kBP). *Radiocarbon* **62**, 725–757 (2020).

56. A. G. Hogg, T. J. Heaton, Q. Hua, J. G. Palmer, C. S. Turney, J. Southon, A. Bayliss, P. G. Blackwell, G. Boswijk, C. B. Ramsey, C. Pearson, F. Petchey, P. Reimer, R. Reimer, L. Wacker, SHCal20 Southern Hemisphere Calibration, 0–55,000 Years cal BP. *Radiocarbon* **62**, 797–778 (2020).

57. S. G. A. Flantua, O. Mottl, K. P. Bhatta, V. A. Felde, T. Giesecke, S. J. Goring, E. C. Grimm, S. G. Haberle, H. Hooghiemstra, S. J. Ivory, P. Kuneš, S. Wolters, A. W. R. Seddon, J. W. Williams, Mottl et al. (2021, Science) Taxonomic harmonization tables for North America, Latin America, Europe, Asia, Africa, figshare (2021); https://doi.org/10.6084/m9.figshare.13049735.v2.

58. D. Fastovich, J. M. Russell, S. T. Jackson, J. W. Williams, Deglacial temperature controls on no-analog community establishment in the Great Lakes Region. *Quaternary Science Reviews* **234**, 106245 (2020).

59. F. Biondi, D. M. Meko, G. Piovesan, Maximum tree lifespans derived from public-domain dendrochronological data. *iScience* **26**, 106138 (2023).

60. S. R. Meyers, "Astrochron: An R package for astrochronology" (manual, 2014); https://cran.r-project.org/package=astrochron.

61. R Core Team, "R: A language and environment for statistical computing" (manual, Vienna, Austria, 2021); https://www.R-project.org/.

62. J. C. Gower, Some distance properties of latent root and vector methods used in multivariate analysis. *Biometrika* **53**, 325–338 (1966).

63. J. T. Overpeck, T. Webb, I. C. Prentice, Quantitative interpretation of fossil pollen spectra - dissimilarity coefficients and the method of modern analogs. *Quaternary Research* **23**, 87–108 (1985).

64. D. G. Gavin, W. W. Oswald, E. R. Wahl, J. W. Williams, A statistical approach to evaluating distance metrics and analog assignments for pollen records. *Quaternary Research* **60**, 356–367 (2003).

65. T. Laepple, P. Huybers, Reconciling discrepancies between Uk37 and Mg/Ca reconstructions of Holocene marine temperature variability. *Earth and Planetary Science Letters* **375**, 418–429 (2013).

66. D. Fastovich, Code and Data for Timescale-dependent response of vegetation to climate change, version 1.0, Zenodo (2024); https://doi.org/10.5281/ZENODO.12726798.

67. J. W. Kirchner, Aliasing in $1/{f}^{\ensuremath{\alpha}}$ noise spectra: Origins, consequences, and remedies. *Phys. Rev. E* **71**, 066110 (2005).

68. R. Hébert, U. Herzschuh, T. Laepple, Millennial-scale climate variability over land overprinted by ocean temperature fluctuations. *Nat. Geosci.*, 1–7 (2022).

69. V. M. R. Muggeo, Estimating regression models with unknown break-points. *Statistics in Medicine* **22**, 3055–3071 (2003).

70. C. Wunsch, The spectral description of climate change including the 100 ky energy. *Climate Dynamics* **20**, 353–363 (2003).

71. M. E. Mann, J. M. Lees, Robust estimation of background noise and signal detection in climatic time series. *Climatic Change* **33**, 409–445 (1996).

72. S. Coats, J. E. Smerdon, S. Stevenson, J. T. Fasullo, B. Otto-Bliesner, T. R. Ault, Paleoclimate Constraints on the Spatiotemporal Character of Past and Future Droughts. *Journal of Climate* **33**, 9883–9903 (2020).

73. S. Minobe, A 50–70 year climatic oscillation over the North Pacific and North America. *Geophysical Research Letters* **24**, 683–686 (1997).

74. D. I. Vyushin, P. J. Kushner, Power-Law and Long-Memory Characteristics of the Atmospheric General Circulation. *Journal of Climate* **22**, 2890–2904 (2009).

75. J. M. Lora, D. E. Ibarra, The North American hydrologic cycle through the last deglaciation. *Quaternary Science Reviews* **226**, 25 (2019).

76. S. A. Marcott, P. U. Clark, L. Padman, G. P. Klinkhammer, S. R. Springer, Z. Y. Liu, B. L. Otto-Bliesner, A. E. Carlson, A. Ungerer, J. Padman, F. He, J. Cheng, A. Schmittner, Ice-shelf collapse from subsurface warming as a trigger for Heinrich events. *Proceedings of the National Academy of Sciences of the United States of America* **108**, 13415–13419 (2011).

77. F. He, J. D. Shakun, P. U. Clark, A. E. Carlson, Z. Y. Liu, B. L. Otto-Bliesner, J. E. Kutzbach, Northern Hemisphere forcing of Southern Hemisphere climate during the last deglaciation. *Nature* **494**, 81–85 (2013).

78. C. Buizert, V. Gkinis, J. P. Severinghaus, F. He, B. S. Lecavalier, P. Kindler, M. Leuenberger, A. E. Carlson, B. Vinther, V. Masson-Delmotte, J. W. C. White, Z. Liu, B. Otto-Bliesner, E. J. Brook, Greenland temperature response to climate forcing during the last deglaciation. *Science* **345**, 1177–1180 (2014).

79. R. F. Ivanovic, L. J. Gregoire, A. Burke, A. D. Wickert, P. J. Valdes, H. C. Ng, L. F. Robinson, J. F. McManus, J. X. Mitrovica, L. Lee, J. E. Dentith, Acceleration of Northern Ice Sheet Melt Induces AMOC Slowdown and Northern Cooling in Simulations of the Early Last Deglaciation. *Paleoceanogr. Paleoclimatology* **33**, 807–824 (2018).

80. S. A. Marcott, T. K. Bauska, C. Buizert, E. J. Steig, J. L. Rosen, K. M. Cuffey, T. J. Fudge, J. P. Severinghaus, J. Ahn, M. L. Kalk, J. R. McConnell, T. Sowers, K. C. Taylor, J. W. C. White, E. J. Brook, Centennial-scale changes in the global carbon cycle during the last deglaciation. *Nature* **514**, 616 (2014).

81. E. Monnin, A. Indermühle, A. Dällenbach, J. Flückiger, B. Stauffer, T. F. Stocker, D. Raynaud, J.-M. Barnola, Atmospheric CO2 Concentrations over the Last Glacial Termination. *Science* **291**, 112–114 (2001).

82. S. C. Brown, T. M. L. Wigley, B. L. Otto-Bliesner, C. Rahbek, D. A. Fordham, Persistent Quaternary climate refugia are hospices for biodiversity in the Anthropocene. *Nat Clim Change* **10**, 244-+ (2020).

83. S. C. Brown, C. Mellin, J. García Molinos, E. D. Lorenzen, D. A. Fordham, Faster ocean warming threatens richest areas of marine biodiversity. *Global Change Biology* **28**, 5849–5858 (2022).

84. D. A. Fordham, F. Saltré, S. Haythorne, T. M. L. Wigley, B. L. Otto-Bliesner, K. C. Chan, B. W. Brook, PaleoView: a tool for generating continuous climate projections spanning the last 21 000 years at regional and global scales. *Ecography* **40**, 1348–1358 (2017).

85. J. R. Petit, J. Jouzel, D. Raynaud, N. I. Barkov, J.-M. Barnola, I. Basile, M. Bender, J. Chappellaz, M. Davis, G. Delaygue, M. Delmotte, V. M. Kotlyakov, M. Legrand, V. Y. Lipenkov, C. Lorius, L. PÉpin, C. Ritz, E. Saltzman, M. Stievenard, Climate and atmospheric history of the past 420,000 years from the Vostok ice core, Antarctica. *Nature* **399**, 429–436 (1999).

86. C. Barbante, J.-M. Barnola, S. Becagli, J. Beer, M. Bigler, C. Boutron, T. Blunier, E. Castellano, O. Cattani, J. Chappellaz, D. Dahl-Jensen, M. Debret, B. Delmonte, D. Dick, S. Falourd, S. Faria, U. Federer, H. Fischer, J. Freitag, A. Frenzel, D. Fritzsche, F. Fundel, P. Gabrielli, V. Gaspari, R. Gersonde, W. Graf, D. Grigoriev, I. Hamann, M. Hansson, G. Hoffmann, M. A. Hutterli, P. Huybrechts, E. Isaksson, S. Johnsen, J. Jouzel, M. Kaczmarska, T. Karlin, P. Kaufmann, S. Kipfstuhl, M. Kohno, F. Lambert, A. Lambrecht, A. Lambrecht, A. Landais, G. Lawer, M. Leuenberger, G. Littot, L. Loulergue, D. Lüthi, V. Maggi, F. Marino, V. Masson-Delmotte, H. Meyer, H. Miller, R. Mulvaney, B. Narcisi, J. Oerlemans, H. Oerter, F. Parrenin, J.-R. Petit, G. Raisbeck, D. Raynaud, R. Röthlisberger, U. Ruth, O. Rybak, M. Severi, J. Schmitt, J. Schwander, U. Siegenthaler, M.-L. Siggaard-Andersen, R. Spahni, J. P. Steffensen, B. Stenni, T. F. Stocker, J.-L. Tison, R. Traversi, R. Udisti, F. Valero-Delgado, M. R. van den Broeke, R. S. W. van de Wal, D. Wagenbach, A. Wegner, K. Weiler, F. Wilhelms, J.-G. Winther, E. Wolff, EPICA Community Members, One-to-one coupling of glacial climate variability in Greenland and Antarctica. *Nature* **444**, 195–198 (2006).

87. D. Kaufman, N. McKay, C. Routson, M. Erb, C. Datwyler, P. S. Sommer, O. Heiri, B. Davis, Holocene global mean surface temperature, a multi-method reconstruction approach. *Scientific Data* **7**, 13 (2020).

88. S. T. Jackson, "Pollen and spores in Quaternary lake sediments as sensors of vegetation composition: theoretical models and empirical evidence" in *Sedimentation of Organic Particles*, A. Traverse, Ed. (Cambridge University Press, Cambridge, 1994; https://www.cambridge.org/core/books/sedimentation-of-organic-particles/pollen-and-spores-in-quaternary-lake-sediments-as-sensors-of-vegetation-composition-theoretical-models-and-empirical-evidence/DCC368064032C32E792D2BBB291EFA36), pp. 253–286.

89. J. D. Hays, J. Imbrie, N. J. Shackleton, Variations in the Earth's Orbit: Pacemaker of the Ice Ages. *Science* **194**, 1121–1132 (1976).

90. A. Berger, Milankovitch Theory and climate. *Reviews of Geophysics* **26**, 624–657 (1988).

91. W. Zhao, P. E. Tarasov, A. V. Lozhkin, P. M. Anderson, A. A. Andreev, J. A. Korzun, M. Melles, E. Y. Nedorubova, V. Wennrich, High-latitude vegetation and climate changes during the Mid-Pleistocene Transition inferred from a palynological record from Lake El'gygytgyn, NE Russian Arctic. *Boreas* **47**, 137–149 (2018).

92. Y. Zhao, P. C. Tzedakis, Q. Li, F. Qin, Q. Cui, C. Liang, H. J. B. Birks, Y. Liu, Z. Zhang, J. Ge, H. Zhao, V. A. Felde, C. Deng, M. Cai, H. Li, W. Ren, H. Wei, H. Yang, J. Zhang, Z. Yu, Z. Guo,

Evolution of vegetation and climate variability on the Tibetan Plateau over the past 1.74 million years. *Science Advances* **6**, eaay6193 (2020).

93. P. C. Tzedakis, Long-term tree populations in northwest Greece through multiple Quaternary climatic cycles. *Nature* **364**, 437–440 (1993).

94. A. L. Berger, Long-Term Variations of Caloric Insolation Resulting from the Earth's Orbital Elements1. *Quaternary Research* **9**, 139–167 (1978).

95. J. Imbrie, A. Berger, E. A. Boyle, S. C. Clemens, A. Duffy, W. R. Howard, G. Kukla, J. Kutzbach, D. G. Martinson, A. McIntyre, A. C. Mix, B. Molfino, J. J. Morley, L. C. Peterson, N. G. Pisias, W. L. Prell, M. E. Raymo, N. J. Shackleton, J. R. Toggweiler, On the structure and origin of major glaciation cycles 2. The 100,000-year cycle. *Paleoceanography* **8**, 699–735 (1993).

96. C. J. F. ter Braak, Canonical Correspondence Analysis: A New Eigenvector Technique for Multivariate Direct Gradient Analysis. *Ecology* **67**, 1167–1179 (1986).

97. D. B. Percival, A. T. Walden, *Spectral Analysis for Physical Applications* (Cambridge University Press, ed. 1, 1993; https://www.cambridge.org/core/product/identifier/9780511622762/type/book).

98. E. C. Ellis, J. O. Kaplan, D. Q. Fuller, S. Vavrus, K. Klein Goldewijk, P. H. Verburg, Used planet: A global history. *Proceedings of the National Academy of Sciences* **110**, 7978–7985 (2013).

99. E. Dinerstein, D. Olson, A. Joshi, C. Vynne, N. D. Burgess, E. Wikramanayake, N. Hahn, S. Palminteri, P. Hedao, R. Noss, M. Hansen, H. Locke, E. C. Ellis, B. Jones, C. V. Barber, R. Hayes, C. Kormos, V. Martin, E. Crist, W. Sechrest, L. Price, J. E. M. Baillie, D. Weeden, K. Suckling, C. Davis, N. Sizer, R. Moore, D. Thau, T. Birch, P. Potapov, S. Turubanova, A. Tyukavina, N. De Souza, L. Pintea, J. C. Brito, O. A. Llewellyn, A. G. Miller, A. Patzelt, S. A. Ghazanfar, J. Timberlake, H. Klöser, Y. Shennan-Farpón, R. Kindt, J.-P. B. Lillesø, P. Van Breugel, L. Graudal, M. Voge, K. F. Al-Shammari, M. Saleem, An Ecoregion-Based Approach to Protecting Half the Terrestrial Realm. *BioScience* **67**, 534–545 (2017).

100. W. R. Peltier, Global glacial isostasy and the surface of the ice-age Earth: the ICE-5G (VM2) model and GRACE. *Annual Review of Earth and Planetary Sciences* **32**, 111–149 (2004).

Science
AAAS

Supplementary Materials for

Coupled, decoupled, and abrupt responses of vegetation to climate across timescales

David Fastovich, Stephen R. Meyers, Erin E. Saupe, John W. Williams, Maria Dornelas, Elizabeth M. Dowding, Seth Finnegan, Huai-Hsuan M. Huang, Lukas Jonkers, Wolfgang Kiessling, Ádám T. Kocsis, Qijian Li, Lee Hsiang Liow, Lin Na, Amelia M. Penny, Kate Pippenger, Johan Renaudie, Marina C. Rillo, Jansen Smith, Manuel J. Steinbauer, Mauro Sugawara, Adam Tomašovỳch, Moriaki Yasuhara, Pincelli M. Hull

Corresponding author: David Fastovich, dfastovi@syr.edu

The PDF file includes:

Materials and Methods

Fossil Pollen Abundances and Age Depth Modeling

We estimate vegetation turnover from fossil pollen abundances stored in geologic archives, such as lacustrine sediments (*51*). Fossil pollen tracks plant assemblage composition through time, albeit with some biases and limitations. Taxonomic resolution is often to the genus level (e.g. *Picea*), though species-level identification is possible (e.g. *Alnus rugosa*) for some fossil pollen morphotypes, and only family-level identification is possible for others (e.g. Poaceae). Additionally, some taxa overproduce pollen and others underproduce pollen relative to the source vegetation assemblage. For instance, pine (*Pinus*) is often overrepresented in pollen assemblages while fir (*Abies*) tends to be underrepresented (*52*). Our analyses account for these production biases by including metrics that downweigh abundant fossil pollen taxa and increase the weight of rarer taxa (e.g. squared chord dissimilarity metric incorporates a square root transform and we square root transform the fossil pollen assemblages before correspondence analysis). When these biases are considered and accounted for in analyses, as we do here, fossil pollen is an effective representation of the source plant assemblage. We refer the reader to Chevalier et al. (*51*) for a comprehensive review of fossil pollen as a proxy for plant assemblage composition.

We gathered fossil pollen abundance data from the Neotoma Paleoecology Database (*8*) in May 2022, which was included as a part of the BioDeepTime database (*9*). For this fossil pollen data aggregation, we searched all fossil pollen records in Neotoma with at least 10 fossil pollen assemblages through time. Our initial search was based on the site list from Mottl et al. (*37*), which compiled 1,181 high-quality fossil pollen records from Neotoma that met our requirements. However, we did not temporally limit our search to 18,000 years as in Mottl et al. (*37*), which produced an additional 181 fossil pollen records, hereafter referred to as "sites". Note, however, that in Neotoma, one site-level sedimentary archive may have multiple fossil pollen records (e.g. if there are multiple cores from a lake or mire). In total, we compiled 1,362 sites with at least 10 observations of a fossil pollen assemblage through time (e.g. at least 10 points in each assemblage time series).

We created age-depth models using Bchron (*53*, *54*) to improve upon existing Neotoma age estimates, which sometimes rely on age-depth models that can underestimate error. Bchron uses information from sparse but specific ages for depths in sedimentary archives for the sites to develop a continuous model of sedimentation from which ages at every depth can be estimated (*54*). An ensemble of possible sedimentation rates is estimated from the chronological controls to generate a posterior distribution of age-depth relationships that allows uncertainty about the age-depth relationship in a sedimentary archive to be propagated to all analyses. Age controls included radiocarbon years, varve years, biostratigraphic markers, and core-top age.

Bchron models were run with default parameters (*54*), except for the radiocarbon calibration curve, which requires hemisphere-specificity to convert radiocarbon years to calendar years due to interhemispheric differences in $^{14}CO_2$ production, uptake, and reservoir effects. Sites in the Northern Hemisphere were calibrated using IntCal20 (*55*) and sites in the Southern Hemisphere were calibrated using SHCal20 (*56*). Non-radiocarbon ages were incorporated into Bchron as calendar years before 1950, with Gaussian errors. Chronological controls with no given age

uncertainties, often the case with biostratigraphic ages, were assigned a Gaussian, one standard deviation, age error that was 10% of the age estimate (e.g. for an age estimate of 1,000 years with no assigned error, the ages followed a N(1000, 100^2) distribution in Bchron). From our compilation, 19 sites had only one chronological control and were excluded from further analyses. Additionally, the Bchron algorithm failed to initialize for five sites that were also excluded.

After creating new age-depth models, we harmonized the taxonomy across these sites using taxa lists from Flantua et al. (*57*). We were not able to match taxa in Flantua et al. (*57*) for 21 sites, so these sites were removed from further analyses. Of these removed sites, 16 were in Oceania and Australia because the taxonomy harmonization lists from Flantua et al. (*57*) do not include these regions. Lastly, one site (Foy Lake, Data S1) contained negative abundances for some fossil pollen counts and was removed from further analyses. Five sites had issues with both chronological controls and taxonomy harmonization, therefore the final compilation of fossil pollen abundances included 1,321 datasets with good spatiotemporal coverage (Data S1). Sites span the Southern Hemisphere midlatitudes to the Northern Hemisphere Arctic, with the densest sampling between 40° N and 50° N, and the least dense sampling between 20° S and 50° S (Fig. S1). Although we perform analyses on tropical/extra-tropical averages, the abundance of temperate midlatitude sites may make globally averaged results more sensitive to temperature, especially considering that these sites demonstrate strong responses to past temperature changes (e.g. Bonnett Lake in *58*). The Northern Hemisphere is better represented across sites than the Southern Hemisphere.

Temporally, these records span the last 600,000 years, with one site spanning an interval from 1.4 to 1.5 Ma, and they are heavily concentrated in the last 20,000 years (Fig. S1). Based on the median age-depth model for each site, 389 sites have a temporal span less than 10,000 years, 746 sites have a temporal span between 10,000 to 20,000 years, 72 have a temporal span between 20,000 to 30,000 years, 43 have a temporal span between 30,000 to 40,000 years, 17 have a temporal span between 40,000 to 50,000 years, 19 have a temporal span between 50,000 to 60,000 years, seven have a temporal span between 60,000 to 70,000 years, six have a temporal span between 70,000 to 80,000 years, three have a temporal span between 80,000 to 90,000 years, one has a temporal span between 90,000 to 100,000 years, and 18 have a temporal span greater than 100,000 years. Of this final compilation, seven sites had different fossil pollen assemblages at identical depths (Dataset IDs: 22,636, 22,797, 3,973, 4,196, 4,197, 4,7975, 525 in Data S1). For each duplicate depth, we retained the first entry.

Tree Longevity Estimates

We estimated tree longevity with observations from all taxa available in the International Tree Ring Data Bank (ITRDB) (*35*, *36*). We gathered all tree ring width records and retained tree ring collections where at least one tree ring record spanned 90% of the tree-ring collection chronology, to minimize underestimation and overestimation of longevity (*24*). We used the longest tree ring record in a collection to estimate longevity for that collection and report the median across all collections in the main text (*59*). The spatial distribution of the ITRDB is comparable to the fossil pollen sites, which have the greatest density of tree ring width records in North America and Europe and comparatively fewer records in the Southern Hemisphere (Fig.

S1) (*36*). The ITRDB lacks records in the tropics, but our median estimate of tree longevity (246 years) agrees with a compilation of tree ring width records from the tropics (*24*).

Spectral Analysis

We used Thomson's multitaper method (MTM) (*17*) to estimate the power spectra of fossil pollen turnover using the *astrochron* R-package (R version 4.4.2, *astrochron* version 1.4) (*60*, *61*). MTM is a Fourier-based method that reduces spectral bias (e.g., spectral leakage) through the application of multiple orthogonal data "tapers" that weigh a time series according to Slepian functions (*17*), of which we used five 3π prolate tapers. The application of Slepian data tapers imparts several positive attributes to MTM when compared to the standard discrete Fourier transform: a reduction in spectral leakage and optimal bias protection for a specified bandwidth resolution, and leveraging of the multiple tapers to provide a statistical sample for estimation of spectral power and its uncertainty (*17*). We scale spectral estimates from MTM by energy per unit frequency to return power spectral density, hereafter referred to as the power spectrum (*5*). An underlying assumption in these analyses, and all spectral analyses, is that a single power spectrum is a good representation of the entire time series.

We further processed the fossil pollen abundances to meet the MTM requirements of a univariate, regularly sampled time series. We addressed the requirement of a single time series by using principal coordinate analysis (PCO) (*62*) on fossil pollen dissimilarity matrices to reduce the dimensionality of the fossil pollen abundances. Pollen dissimilarity matrices were calculated for each individual time series using the squared chord distance metric (*63*), which consistently outperforms other distance metrics in distinguishing between two distinct fossil pollen assemblages (*63*, *64*). We retained the primary (PCO1) and secondary (PCO2) dimensions of variability for further analysis via MTM and presented the results from the primary dimension of variability in the main manuscript (Fig. S2).

We sought to identify latitudinal differences in fossil pollen dissimilarity, for comparison with climate variables which are known to have a variance structure that varies by latitude (*5*). To that end, we multiplied PCO1 by the square root of its corresponding eigenvalue. This procedure scales PCO1 for each fossil pollen assemblage by the variance explained by that dimension. That is, a fossil pollen assemblage where PCO1 explains a substantial amount of compositional variance will have a large eigenvalue corresponding to PCO1 and PCO1 will be up-weighted, producing high spectral energy across all frequencies. In contrast, a fossil pollen assemblage where PCO1 explains little variance will have a small eigenvalue corresponding to PCO1 and PCO1 will be down-weighted. Total spectral energy (i.e. area under a power spectral density spectrum) is equal to the variance of the time series (Parseval's theorem). Therefore, any spatial patterns in the variance explained by PCO1 are imprinted onto the time series and will produce high spectral power when PCO1 is up-weighted and low spectral power when PCO1 is down-weighted. This effect carries forward to spatially averaged power spectra (i.e. tropical and extra-tropical averaged power spectra) thereby enabling an assessment of whether there are spatial patterns in fossil pollen turnover.

Temporal sampling that is evenly spaced (i.e. identical temporal distance between all consecutive samples) is required by MTM, but this condition is rarely met by proxy data extracted from

947 geologic archives. Therefore, we interpolated PCO1 of all fossil pollen assemblages using a
948 linear interpolation approach adapted from (*65*). This approach aims to determine an optimal
949 interpolation resolution and minimize energy loss at high frequencies by comparing the PCO1
950 power spectra to the power spectra of a power law process where $\beta = 1$. The optimal
951 interpolation resolution is identified when the ratio between the theoretical and empirical power
952 spectra crosses 0.7 (*65*). This approach objectively determines an optimal interpolation
953 resolution and includes filtering to minimize the aliasing of high frequency variance that is often
954 present in sedimentary archives (implemented in the new *astrochron* function 'linterpLH13') and
955 present in the Zenodo data repository (*66*)).
956
957 We estimated the power spectra of global ecological turnover by performing MTM on PCO1 for
958 individual sites after subtracting the mean from each site-level PCO1 time series, then bin
959 spectral power by log10(frequency), and average spectral power across sites within each
960 frequency bin. This choice was made to avoid convoluting temporal and spatial variance in the
961 eigenvector decomposition of the community dissimilarity matrix, as would have occurred if we
962 considered all sites and samples together. By averaging power spectra across sites, we leverage
963 both short, highly-sampled records to resolve high frequencies and long, sparsely-sampled
964 records to resolve low frequencies – characteristics that would be difficult to achieve using any
965 single site's power spectrum alone. For averaging site-level power spectra, we used a bin size of
966 0.01 in log10(frequency) coordinates, which equates to $22{,}000^{-1}$ $years^{-1}$ near the smallest
967 frequencies (e.g. $10^{-6} – 10^{-5.99}$ $years^{-1}$) and <1 year near the largest frequencies (e.g. $10^{0.99} – 10^{1}$
968 $years^{-1}$).
969
970 After estimating the power spectra of global vegetation turnover we evaluated the continuum of
971 global vegetation turnover for specific frequency bands using an ordinary least squares linear
972 regression in log-log space for frequencies resolved by at least two sites (*5*, *6*). Prior to the
973 regression, we smoothed the spatially averaged power spectra using a Gaussian kernel in log10
974 frequency coordinates with a width of 0.03 (*67*, *68*). Using the smoothed global estimate of
975 spectral power for global vegetation turnover, frequency is a predictor of spectral power and the
976 resulting slope is the β exponent in the $S(f) \propto f^{-\beta}$ power law relationship (*5*, *6*). To determine the
977 frequency bands of distinct temporal scaling regimes in spectral power for global vegetation
978 turnover we identified breakpoint locations in the log-log relationship between spectral power
979 and frequency through piecewise linear regressions in the *segmented* R package (version 2.1.3)
980 (*69*). We constrained segmented regressions to identify three breakpoints (low, intermediate, and
981 high frequencies) for fossil pollen turnover and one breakpoint for simulated temperature and
982 precipitation. The number of breakpoints was based on prior expectations for climate (*5*, *6*) and
983 visual inspection for fossil pollen. Although the number of breakpoints is constrained in the
984 segmented regressions, the location of these breakpoints depends on the power spectrum. For
985 vegetation turnover, β was then fit across the four frequency ranges between the three identified
986 breakpoints: (1) the lowest frequency resolved and the low frequency breakpoint, (2) the low
987 frequency breakpoint and the intermediate frequency breakpoint, (3) the intermediate frequency
988 breakpoint and high frequency breakpoint, and (4) the high frequency breakpoint to the highest
989 frequency that produces unbiased estimates of β (see *Estimating the Highest Resolvable*
990 *Frequency for Spectral Analyses*). For example, if a breakpoint in the log-log relationship
991 between spectral power and frequency was identified at 115^{-1} $years^{-1}$, 600^{-1} $years^{-1}$, and $4{,}000^{-1}$
992 $years^{-1}$, β was fit between (1) the lowest frequency resolved and $4{,}000^{-1}$ $years^{-1}$, (2) from $4{,}000^{-1}$

993 years^{-1} and 600^{-1} years^{-1}, (3) from 600^{-1} years^{-1} to 115 years^{-1}, and (4) from 115 years^{-1} to the
994 highest frequency that produces unbiased estimates of β. For temperature and precipitation, we
995 fit β between the lowest frequency resolved and the one breakpoint identified and again from the
996 one breakpoint identified to the highest frequency that produces unbiased estimates of β.
997
998 Within a time series, β characterizes memory (i.e. temporal autocorrelation) and how variance is
999 partitioned across frequencies (*70*). If the exponential coefficient (β) of the power-law
1000 relationship between frequency and spectral power is small (β ~ 0), variance is equally
1001 partitioned among all frequencies (i.e., white noise; Fig. S7) (*70*). In contrast, β > 0 indicates
1002 more variance at lower frequencies (longer periods), with β = 2 defining a random walk (i.e., red
1003 noise; Fig. S7) (*70*). The climate system contains two scaling regimes: small, uncorrelated
1004 variability with a low β and large, autocorrelated variability with a high β. The small, stochastic,
1005 uncorrelated variability of the climate system is present in frequencies as low as 100^{-1} to 1,000^{-1}
1006 years^{-1} (*5*, *6*) and encompasses "weather" components of the climate system (*29*). At lower
1007 frequencies, β increases as slowly responding, coupled components of the "climate" system
1008 increase the magnitude of climate fluctuations while also imparting high autocorrelation (*29*).
1009 Here, the terms "climate" and "weather" delineate these two scaling regimes (*29*).
1010
1011 Recently, methods for estimation of temporal scaling in time series were compared for their
1012 ability to reproduce β in synthetic paleoclimate time series with known β and performed
1013 reasonably well (*33*). In these analyses, MTM emerged biased towards larger β values when
1014 evaluating the full frequency range, compared to other spectral transformation methods (*33*).
1015 However, MTM showed little bias at long timescales (greater than nine times the mean
1016 resolution), moderate bias at intermediate timescales (greater than 4 times the mean resolution),
1017 and generally outperformed competing methods such as spectral transformation from the Lomb-
1018 Scargle periodogram when β is high and the input data is irregularly sampled (*33*). Only Haar
1019 structure functions more accurately estimated β from the synthetic dataset, but the approach is
1020 limited to -1 < β < 3 (*33*) and does not allow for the identification/influence of
1021 quasiperiodic/periodic signals that may bias estimates of the spectral continuum (*71*).
1022 Additionally, MTM has seen broad use in paleoclimatology (*5*, *68*, *72*) and atmospheric sciences
1023 (*73*, *74*) for estimating β, providing baseline estimates for comparison with our study.
1024
1025 <u>TraCE-21ka and Proxy Paleoclimate Estimates</u>
1026
1027 TraCE-21ka is a series of fully coupled climate model experiments that simulate the effect of
1028 transient climate forcings of the most recent deglaciation with the Community Climate System
1029 Model, version 3 (*18*, *19*). Components of the Community Climate System Model, version 3
1030 include the Portable Ocean Model, Community Land Model, and Community Sea Ice Model
1031 (*18*). The climate simulations have a nominal horizontal resolution of 3.75° with 26 vertical
1032 levels (*18*). Surface elevation was averaged within each grid cell resulting in an imperfect
1033 representation of mountain ranges that only span several grid cells, such as the Andes (Fig. S4).
1034 TraCE-21ka includes transient changes in ice sheet topography, meltwater forcing, orbital
1035 configuration, and greenhouse gas concentration that matched then-current proxy reconstructions
1036 (*18*, *19*). These climate simulations have been pillars of paleoclimatological research and have
1037 undergone substantial comparisons against proxy reconstructions and generally perform well
1038 (*18*, *19*, *75–78*). Unlike proxy-based climate reconstructions, TraCE-21ka offers full fields that

are annually resolved and well-suited for comparison against spectral estimates from fossil pollen. For climate parameters such as precipitation, while proxy-based reconstructions remain challenging to develop, physically plausible simulations provide valuable and insightful tools for understanding historical patterns. Temperature and precipitation anomalies for the TraCE-21ka simulation relative to 1850 to 1900 CE baseline are presented in Fig. S5 and Fig. S6.

TraCE-21ka has known deficiencies such as seasonal precipitation biases in North America (*75*) and imperfect greenhouse gas and meltwater forcings (*79–81*). Precipitation is particularly challenging to simulate for all climate models because processes like raindrop formation and convection occur at a sub-grid scale. What's more, all climate models overestimate high frequency climate variability and underestimate low frequency climate variability at local and regional scales (*31*), but our low-pass filtering procedure (summarized below) partially mitigates this climate model limitation by reducing high frequency variability. Nonetheless, TraCE-21ka remains the most comprehensive set of paleoclimatic simulations for the last deglaciation, which are widely used to assess ecological relationships to paleoclimate (*82–84*). Recently, the TraCE-21ka experiments were the first climate simulations to show a scaling break in the continuum of mean global temperature that is expected to exist given physical principles (*6*). For climate parameters like precipitation, simulations

We averaged monthly near-surface temperature (2 m) and total precipitation rate into annual averages. We sought to make direct comparisons between power spectra of simulated temperature, simulated precipitation, and vegetation turnover and therefore degraded the TraCE-21ka climate simulation to match the spatial and temporal characteristics of the fossil pollen sites. Specifically, we subsampled TraCE-21ka spatially to get the nearest grid cell for every fossil pollen site and applied a low-pass filter with a characteristic timescale of twice the mean resolution of the corresponding fossil pollen record to guard against aliasing of high-frequency variance (*33*, *68*). We then downsampled these low-pass filtered climate time series temporally, retaining only the years with fossil pollen data. This process produced a dataset of simulated temperature and precipitation that matched fossil pollen abundances in space and time with similar temporal characteristics (i.e. low-pass smoothing induced by sedimentation). Finally, we interpolated the simulated temperature and precipitation to a regular temporal grid using the same methodology applied to the fossil pollen data (*65*). All spectral analyses for TraCE-21ka were performed on these spatiotemporally subsampled and interpolated temperature and precipitation time series.

For subsampling of the TraCE-21ka simulations, we excluded those fossil pollen samples that were outside of the temporal coverage of TraCE-21ka. Fossil pollen sites that did not contain any fossil pollen assemblage observations within the last 21,000 years were excluded and are not represented in the spectral estimates of the TraCE-21ka simulations.

To capture climate variability outside of the last 21,000 years we supplement our analysis of TraCE-21ka with two empirical proxy records that approximate global temperature variability for the last two million years. We use temperature reconstructions from the EPICA Dome C ice core in Antarctica (*28*). Temperature reconstructions from Antarctic ice cores primarily track global greenhouse gas concentrations and therefore global temperature changes (*85*). We also use global average surface temperature (GAST) reconstructions from Snyder (*20*). This estimate

of GAST is based on proxy-based sea surface temperature reconstructions (SST) that are scaled to surface air temperatures with a value determined by examining SST-surface air temperature differences from the Paleoclimate Modelling Intercomparison Project (PMIP) model simulations. Comparisons between GAST reconstructions, EPICA Dome C, and greenhouse gasses demonstrate that both sets of proxy records used here well approximate global climate evolution (*20*). Variations in ocean circulation emerge in EPICA Dome C oxygen isotopes (*86*) but as a second-order feature imposed on greenhouse gas-controlled temperature changes. The spectral continuum of temperature variability at EPICA Dome C and global surface air reconstructions were fit between 100^{-1}-$15{,}000^{-1}$ years^{-1} (*5*) and $2{,}000^{-1}$-$100{,}000^{-1}$ years^{-1} (*6*), respectively.

Benchmarking TraCE-21ka Simulated Climate Variability Against Temperature12k

We compared TraCE-21ka to the Temperature12k database (*87*), a global compilation of proxy temperature reconstructions that span the last 12,000 years. Note that several proxy reconstructions within Temperature12k extend well beyond the last 12,000 years. We first filtered the Temperature12k database to remove all pollen-based temperature estimates and then estimated the continuum of global temperature variability using the same framework defined in the *TraCE-21ka and Proxy Paleoclimate Estimates* and *Spectral Analyses* section. That is, we estimated power spectra for Temperature12k at a site level, and then averaged across sites to produce a globally averaged power spectrum. For TraCE-21ka, we performed the same procedure after spatiotemporally subsampling and low-pass filtering the temperature simulations. Six of the non-pollen temperature estimates in Temperature12k failed spectral analyses for various reasons (Table S8). No similar comparisons are made for precipitation due to the lack of an analogous database to Temperature12k. However, low-frequency precipitation variability in TraCE-21ka likely results from thermodynamic effects of temperature changes (Clausius-Clapeyron relationship) given the nearly identical power spectra presented in Fig. 2.

We find that TraCE-21ka can accurately simulate the three key features of the temperature continuum: 1) a high β at low frequencies (climate regime), 2) a low β at high frequencies (weather regime), and 3) a breakpoint in the scaling relationship between spectral power and frequency (Fig. S3). In the low frequency, climate, regime, β for Temperature12k is 1.83 and TraCE-21ka simulates a β of 1.87. In the high frequency, weather, regime Temperature12k has a β of 0.54 while TraCE-21ka has a β of -0.25. The location of the break in the scaling relationship for Temperature12k is 376^{-1} years^{-1} and 498^{-1} years^{-1} for TraCE-21ka. These results demonstrate that TraCE-21ka performs well, despite the general struggle of climate models to accurately simulate temporal persistence in the high frequency, weather, regime. Much like other comparisons between empirical climate observations against climate models, TraCE-21ka poorly simulates temporal persistence in temperature variability (i.e. lower β in TraCE-21ka) in the high frequency regime (*31*). Despite this deficiency, TraCE-21ka captures the key features of the temperature continuum and is well-suited as a climate benchmark against which we can compare our globally averaged power spectra of vegetation turnover.

Estimating the Highest Frequency for Unbiased Estimates of β

In light of the limitations and biases of MTM for estimating β (*33*), we sought to estimate the highest frequency that produces unbiased estimates of β for each of our spatially averaged power

spectra. We used the undegraded, annually resolved TraCE-21ka near-surface temperature time series, from the closest grid cell corresponding to each fossil pollen site, as a target signal with a known power spectrum. We then temporally degraded the TraCE-21ka near-surface temperature as outlined in the *TraCE-21ka and Proxy Paleoclimate Estimates* section and compared these degraded power spectra to the undegraded target (annually resolved) signal to estimate the highest frequency where estimates of β are unbiased by sedimentary processes.

In our analyses and prior work (*6*), annually resolved near-surface temperature estimates from TraCE-21ka produce a power spectrum where spectral power is evenly distributed in a high frequency band ($> 672^{-1}$ $year^{-1}$ from Fig. 2). At frequencies lower than this breakpoint, temperature variability increases with frequency (*6*) (Fig. S8). This pattern holds when averaged across all fossil pollen sites (global estimate in Fig. S8), the extra-tropics (extra-tropical estimate in Fig. S8), and the tropics (tropical estimate in Fig. S8). Built upon the expectation that sedimentary processes such as sediment mixing (*88*), and sampling resolution, can decrease spectral power at the highest frequencies and increase β (*33*), we use the even distribution of spectral power in the high frequency band of the undegraded TraCE-21ka temperature power spectrum as the metric to identify when estimates of β become biased by sedimentary processes. We find that high frequency spectral power decreases in the degraded TraCE-21ka power spectra and β increases in all spatial averages (Fig. S8). However, the temporal sampling characteristics of fossil pollen sites in each spatial average vary, leading to a spurious decrease in spectral power and an increase in β at the highest frequencies that varies across the spatial averages. The high latitudes are well represented in our fossil pollen compilation with several short, fossil pollen records with very high resolution (Fig. S1). Therefore, in the degraded global and extra-tropical average power spectra of temperature, β in the high frequency regime is unbiased up to a frequency of 58^{-1} and 57^{-1} $years^{-1}$, respectively (Fig. S8). Above this frequency, there is a spurious decrease in spectral power and an increase in β (Fig. S8). In contrast, tropical fossil pollen sites in our compilation are less well temporally resolved than the extra-tropics, which decreases the frequency where a spurious decrease in spectral power and increase in β begins to 160^{-1} $years^{-1}$ (Fig. S8). Therefore, we fit β to frequencies lower than 58^{-1}, 57^{-1}, and 160^{-1} $years^{-1}$, in all analyses for global, extra-tropical, and tropical power spectra, respectively.

Statistical Comparisons between Estimated Parameters from Spectral Analyses

We compared all estimated parameters (β, break location) from our ensembles of averaged power spectra for temperature, precipitation, and vegetation turnover using two-sided Fisher-Pitman permutation tests. A permutation test is used to determine whether the difference between two groups is statistically significant, without making assumptions about the underlying distribution of the data. In our analysis, we use permutation tests to compare the medians of the estimated parameters between different variables (e.g., temperature vs. vegetation turnover). The process works as follows:

1. We calculated the observed difference in medians between the two groups.
2. We then randomly reassigned the data points to the two groups and recalculated the difference in medians.
3. This process is repeated 10,000 times to create a distribution of possible differences under the null hypothesis of no true difference between groups.

4. We compare our observed difference to this distribution. If the observed difference falls in the 2.5% tails on either side, we consider the difference statistically significant at the 0.05 level.

This approach allows us to assess whether the observed differences in our spectral parameters are likely to have occurred by chance. We report the results of all these comparisons in Table S3 to Table S7.

We also test when estimated parameters are significantly different from 0 (and 2 for β) based on the confidence interval for the median parameter estimate across the ensemble for each parameter (Table S1). We calculated confidence intervals by bootstrapping the median. That is, each ensemble of parameter estimates was randomly resampled with replacement and the median was calculated for this random resample. This procedure was repeated 10,000 times to return a distribution of median estimates for each parameter. From this distribution of bootstrapped median estimates, we report the 2.5% and 97.5% percentiles as the 95% CI.

Methodological Constraints on Milankovitch Signal Detection

Milankovitch cycles are a primary control of global climate (*89*, *90*) and have been identified in fossil pollen records that span the last 2,000,000 years (*91*, *92*). Our analyses demonstrate increased spectral power associated with precession cycles at $21{,}000^{-1}$ years^{-1} in all spatially averaged power spectra but high spectral power in the obliquity band ($41{,}000^{-1}$ years^{-1}) is missing and high spectral power in the eccentricity band ($100{,}000^{-1}$ years^{-1}) is only present in the vegetation turnover power spectrum for tropical sites (Fig. 3). We find that these missing periodicities result from 1) our dimensionality reduction procedure (i.e. PCO), 2) the spatial scale of our compilation, 3) few sites that span enough time to resolve variability in the Milankovitch bands, and 4) variable temporal resolution of the data at each of these few sites.

Individual taxa or groups of taxa often demonstrate periodicity (as seen with arboreal pollen in (*91*) and (*92*)), but when all taxa are included in the dissimilarity matrix for PCO, as we do here, periodicity becomes less pronounced. The Ioannina dataset demonstrates this well (Dataset ID: 4112) (*93*). *Pinus* pollen at Ioannina has a strong cyclical pattern (*93*), but this is weakened when additional taxa are considered when calculating the dissimilarity matrix for PCO (Fig. S13). Evidence of this is visible in Taner-filtered relative abundances for the three most abundant taxa at Ioannina. *Pinus*, *Quercus*, and Poaceae all show variability in the precession, obliquity, and eccentricity bands but all are out of phase (Fig. S13). When MTM is performed on *Pinus* relative abundance a periodic signal between the obliquity and precession bands is present. However, performing MTM on the primary dimension of variability for a dissimilarity matrix created using *Pinus* and *Quercus* relative abundances demonstrates a decrease in this periodic signal because of the antiphase changes in *Pinus* and *Quercus* abundances (Fig. S13). The loss of spectral power in *Pinus* between the obliquity and precession bands is further diminished when Poaceae and *Quercus* are included in the dissimilarity matrix calculation (Fig. S13). When averaging across a global compilation of sites with variable temporal data resolution, 41,000 and 100,000 year periodicities decrease in amplitude, even though individual sites demonstrate periodicity in these bands (e.g. ODP Site 658 (41194) and Páramo de Agua Blanca (21978) in Fig. S14A). As site-level power spectra are averaged to form an estimate of the global power spectrum, high spectral

power in the Milankovitch bands decreases even though it is present at individual sites (Fig. S14B). We hypothesize that high spectral power at $21{,}000^{-1}$ $years^{-1}$ remains because we have more sites with a temporal span and sufficient data resolution that can resolve the 21,000 year periodicity, as compared to the 41,000 and 100,000 year periodicities (Data S1). The limited number of observations from high latitudes (> 65 °N), where obliquity effects are expected to be the dominant mode of variability (*94*), may also explain why we detect precession but not obliquity signals in our spatial distribution of sites. In addition, precession has had a large influence on summer insolation over the last 400,000 years (*95*), which may also partly explain a clear precession signal and the absence of obliquity and eccentricity signals.

Uncertainty Estimation

We quantified uncertainty in our estimates of spectral power and the spectral continuum through Monte Carlo resampling of sites and Bchron posterior age estimates. Specifically, we drew 1,000 sites from our global compilation of 1,321 sites at random, and for each site, we drew a single posterior age estimate for MTM. We then downsampled TraCE-21ka accordingly, as described in the *TraCE-21ka and Proxy Paleoclimate Estimates* section, and then performed MTM as described in the *Spectral Analysis* section. We repeated this procedure 1,000 times, which produced an ensemble of 1,000 estimates of global spectral power, β, and breakpoint locations, for climate and fossil pollen turnover, from which we reported the median and 95% confidence interval (Fig. S21, Fig. S22, Table S1). All sampling was performed using a uniform distribution without replacement. This uncertainty estimation procedure assesses the influence of age model uncertainty and site selection on the global and latitudinally averaged power spectra.

Sensitivity Tests

We assessed the sensitivity of our results to our choice of fossil pollen dimensionality reduction, power spectra estimation methods, spatial averaging, and anthropogenic land use change (Fig. S9, Fig. S10, Fig. S11, Fig. S12, Fig. S15, Fig. S16). For dimensionality reduction, we tested alternative methods to reduce fossil pollen dimensionality and various community dissimilarity metrics. In these sensitivity tests, we calculated community dissimilarity using the Bray Curtis and Jaccard dissimilarity metrics. We also performed correspondence analysis after square root transforming the fossil pollen assemblages, which, unlike PCO, does not assume linearity (*96*). Lastly, to test the sensitivity of our analyses to fossil pollen analytical accuracy, we degraded the percent abundance fossil pollen observations to presence/absence, though the Jaccard distance metric is presence/absence based as well.

Changing the dissimilarity metric and the dimension of variability analyzed had limited impacts on our conclusions, however, correspondence analyses produced results with the least total spectral power (Fig. S9, Fig. S10). We hypothesize that this occurs because PCO assumes linearity in the species-matrix decomposition while correspondence analysis does not assume linearity (*96*). Correspondence analysis also produced slightly different results for latitudinally averaged power spectra because of the scaling procedure we implemented (Fig. S11, Fig. S12). The eigenvalues in correspondence analyses do not indicate variance explained as they do in PCO. Rather, eigenvalues correspond to correlation coefficients between the coordinates for species in the fossil pollen assemblage (i.e. species score) and coordinates for time intervals (i.e.

site score) in the ordination coordinate system. However, our scaling procedure, which assumes that the eigenvalues correspond to the variance explained, is incompatible with correspondence analysis. Nevertheless, we include sensitivity tests for correspondence analysis to assess the assumption of linearity in PCO and the influence of metric saturation on our results. We chose to present the first dimension from PCO using the squared chord distance metric because of strong support for the efficacy of the squared chord distance metric to discriminate fossil pollen assemblages that source from distinct ecosystems (*63*, *64*).

We also tested different methods for estimating the global spectral continuum of vegetation turnover by taking the mean of MTM adaptive spectral power (as shown in the main text), taking the median of MTM adaptive spectral power, averaging MTM spectral eigencoefficients, and averaging β for each site. The methodology for median estimates of MTM adaptive spectral power was identical to the main manuscript except we took the median, not the mean as in the main text. The procedure for returning a global average of spectral power by averaging eigencoefficients was nearly identical to averaging by spectral power. We first performed MTM on a single site and retained the five spectral eigencoefficients for each site that correspond to the five data tapers. We then averaged the five eigencoefficients across all sites by binning by frequency, as described in the *Spectral Analysis* section. We then calculated spectral power at each frequency using the averaged eigencoefficients and Equation 1, where $\hat{S}_k(f)$ is spectral power and $y_k(f)$ is the eigencoefficient for the kth data taper. Since we use five data tapers, this produces five estimates of $\hat{S}_k(f)$ which we average to estimate total spectral power (*17*).

$$\hat{S}_k(f) = |y_k(f)|^2 \quad \text{(Equation 1)}$$

These estimates of total spectral power were used to estimate β. The eigencoefficient averaging provides an important complementary view to the MTM adaptive spectral power approaches noted above, as it explicitly considers the signal phase at each site. That is, strong signals that are antiphased at different locations will cancel, instead of being amplified as the case for the MTM adaptive spectral power approaches. Eigencoefficient averaging is expected to reduce the overall power at a given frequency in the reconstructed spectrum and to diminish periodic signals that are not in phase globally since it allows for destructive interference across sites.

Lastly, we estimated the global continuum of vegetation turnover by directly averaging β at each site. Here, we performed MTM at each site as described in the *Spectral Analysis* section and then estimated β using an ordinary least squares regression in log-log space, retaining β at each site, not spectral power. Estimates of β were then averaged across sites resulting in a global estimate of the spectral continuum of fossil pollen turnover. These sensitivity tests were performed within the same Monte Carlo framework that we use to quantify uncertainty for the fossil pollen assemblages and TraCE-21ka climate parameters.

Our conclusions are robust to the method used to aggregate individual site-level power spectra of vegetation turnover into a global estimate. All four approaches reveal four characteristic timescales in global vegetation turnover each with distinct βs: high β at the highest frequencies, low β in the high-intermediate frequency band, high β in the low-intermediate frequency band, and low β in the low frequency band (Fig. S9). Across much of the frequency space,

uncertainties for these approaches overlap, particularly at high and low frequencies where spectral power estimates diverge.

This divergence is most prominent in two areas: the high and low frequencies. At low frequencies, global estimates that use the mean of site-level power spectra have greater spectral power than estimates that use the median of site-level power spectra and the mean of site-level eigencoefficient estimates (Fig. S9). At high frequencies, global estimates that use the median of site-level power spectra and the mean of site-level eigencoefficient estimates have a band-limited increase in the globally estimated spectral power, not present in the global estimate that uses the mean of site-level power spectra (Fig. S9). These discrepancies may stem from the different underlying distributions of site-level spectral power and eigencoefficient estimates, and the phase relationships that are preserved in the eigencoefficient estimates.

The spectral power estimates from MTM of a Gaussian process follow a chi-square distribution with two degrees of freedom, while the distribution of eigencoefficients approximately follows a normal distribution (*17*, *97*). This suggests that the estimated global power spectra of vegetation turnover using the mean of site-level spectral power should be systematically higher than median estimates and mean of eigencoefficient estimates, while the latter two should be similar. Our sensitivity tests capture this systematic offset (Fig. S9) and explain higher spectral power at low frequencies when using the mean of site-level spectral power. At low frequencies, individual sites with high spectral power pull the global estimate to higher values. While this offset should also exist at high frequencies, we observe a counterintuitive result: individual sites with low spectral power pull the global estimate that uses the mean of site-level spectral power to values comparable to the median and eigencoefficient global estimates (Fig. S9). In light of this unexpected observation, and considering that each approach produces identical conclusions, we present results using the mean of spectral power to maintain consistency with prior studies (*5*, *6*, *68*).

In contrast to the robust conclusions when estimating the globally averaged power spectra of vegetation turnover using the mean, median, and mean of eigencoefficients we find that results were highly sensitive to averaging by β. This is a product of our piecewise regression procedure to determine the location of breaks in the log-log fit between spectral power and frequency in the high and intermediate frequency bands. Accurately identifying the location of breaks in β between the high and high-intermediate frequency bands requires high-resolution sampling which is present in a subset of fossil pollen assemblages (Fig. S9, Fig. S10). Performing breakpoint identification on spectral power at a site level increases the weight of the more abundant lower-resolution sites and reduces the weight of the less abundant high-resolution sites, reducing frequency resolution and biasing estimates of globally averaged β.

We assessed the sensitivity of our conclusions to the influence of anthropogenic land-use change. We performed all analyses after first removing all samples from the last 2,000 years (*32*), the interval during which anthropogenic influences in fossil pollen records are strongly expressed (*37*). Removing any samples within the last 2,000 years produces nearly identical power spectra at frequencies lower than 100^{-1} $years^{-1}$ and suggests that climate tracking at millennial to multi-centennial scales persists (Fig. 2, Fig. S15). However, the detected breakpoints and β change if samples from the last 2,000 years are removed. The high frequency breakpoint (Fig. 2, 149^{-1}

years^{-1}) decreases to 527^{-1} years^{-1} and β decreases from 4.34 to 0.53; the breakpoint at 797^{-1} years^{-1} decreases to 3,602^{-1} years^{-1} and β increases from -0.1 to 1.96; the breakpoint at 18,012^{-1} years^{-1} decreases to 19,946^{-1} years^{-1} and β decreases from 1.84 to 1.09; and β for the lowest frequencies increases from -0.08 to -0.008. Our sampling density increases as age decreases (Fig. S1) and sites with the highest temporal resolution span the last 2,000 years (Data S1), therefore these changes in breakpoints and β may be a result of reduced sampling density. Despite statistically different βs at the highest frequencies, globally averaged power spectra still demonstrate a decrease in spectral power in the high frequency band which is particularly well demonstrated in the confidence intervals, matching results from the main manuscript (Fig. 2, Fig. S15) and results from similar analyses at a continental scale that also remove fossil pollen observations from the last 2,000 years (*32*). This suggests that climate decoupling at the highest frequencies may contain some influence of anthropogenic land use change (*38*, *98*) but this is not the only control on high frequency vegetation turnover.

Lastly, we assessed the sensitivity of our results to our choice of averaging across all sites, sites in the tropics, and sites in the extra-tropics by averaging across biomes from Dinerstein (*99*)(Fig. S17, Fig. S16). Results partially align with expectations given the life history of the primary plant functional types that compose each biome. For instance, biomes with grassland ecosystems such as Montane Grasslands and Shrubland and Tropical and Subtropical Grasslands, Savannas and Shrublands have smaller β's than tree dominated biomes like Temperate Broadleaf and Mixed Forests, Boreal Forests/Taiga, and Mediterranean Forests (Fig. S16). Grasslands have a shorter lifespan and would be expected to have a lower β at high frequencies unlike tree-dominated ecosystems which have increasing turnover approaching the median age of tree longevity (Fig. 2). However, β remains low across most frequencies, not just high frequencies. This may occur because grass pollen is commonly identifiable to the family level, therefore any changes in grassland composition are not observed by fossil pollen and may lead to low vegetation turnover at low frequencies (Fig. S16). However, the Tundra and Temperate Conifer Forests do not cohere with these expectations. Temperate Conifer Forests have a low β and a power spectrum that is characterized by abrupt changes indicated by high spectral power at ~5,000^{-1} and ~9,000^{-1} years^{-1}. In contrast, the Tundra biome has a large β despite being composed primarily of dwarf shrubs and grasses, with short generation times. Despite these two exceptions, β and power spectra averaged across biomes generally align with ecologic expectations.

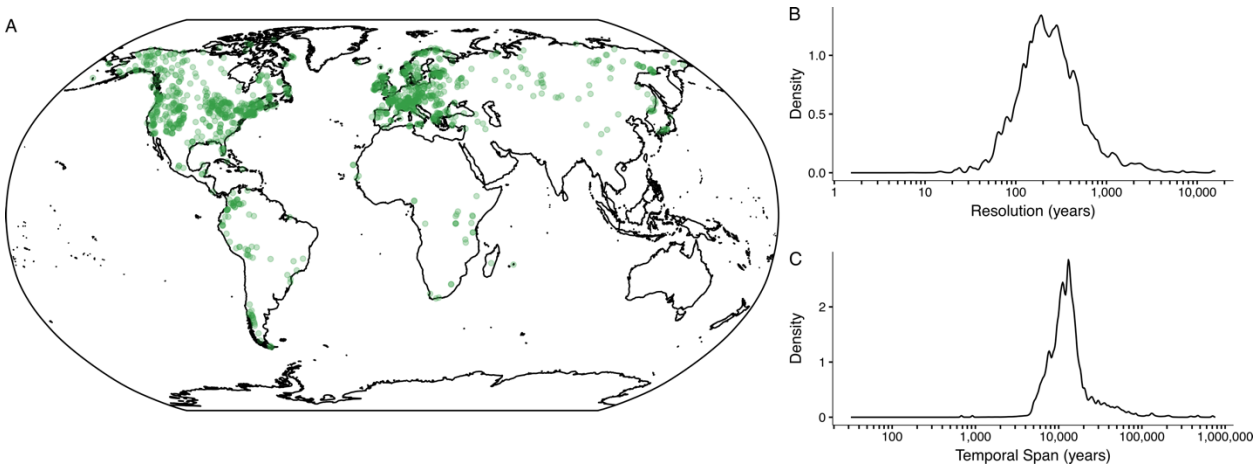

Fig. S1

(A) All sites used in the spectral analyses, as in Fig. 2A. The probability density of (B) temporal resolution and (C) temporal span for all sites analyzed and all corresponding posterior age estimates. Note, that the Northern Hemisphere is more well-represented than the Southern Hemisphere.

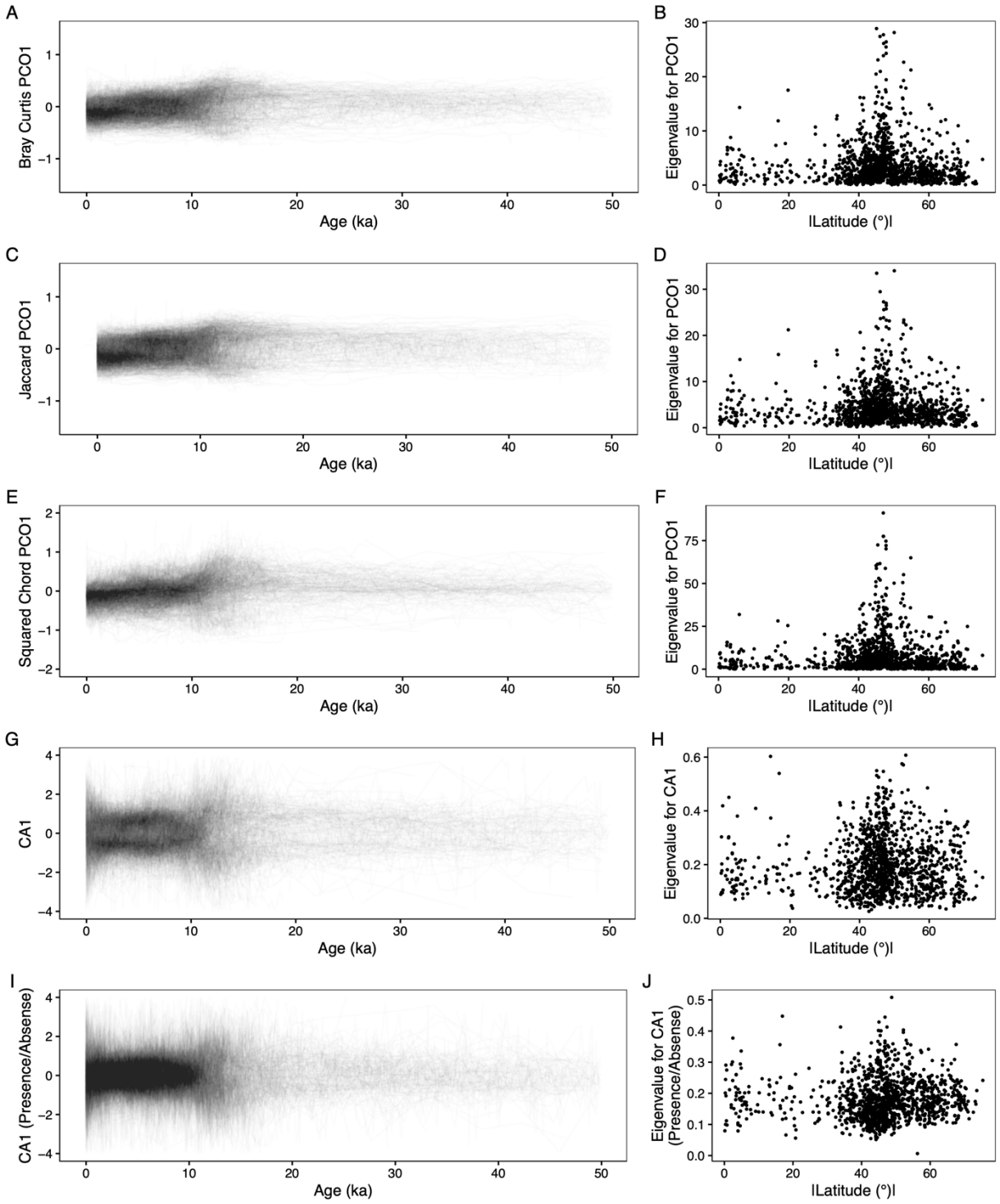

1403

1404 **Fig. S2**

1405 (A, C, E, G, I) The primary dimension of variability from 1) principal coordinates analyses
1406 (PCO) using the (A) Bray-Curtis, (C) Jaccard, and (E) Squared Chord Distance metrics and 2)
1407 (G) correspondence analysis on fossil pollen assemblages for each site analyzed. We also
1408 performed correspondence analyses on fossil pollen assemblages after degrading the abundance

observations to presence/absence (I). (B, D, F, H, J) Eigenvalues corresponding to PCO1 for each site plotted against the absolute value of the site latitude. For correspondence analyses, eigenvalues do not correspond to variance explained as they do for principal coordinate analyses. Rather, eigenvalues correspond to correlation coefficients between the coordinates for species in the fossil pollen assemblage (i.e. species score) and coordinates for time intervals (i.e. site score) in the ordination coordinate system. For visual simplicity, the PCO1 and CA1 results for each site are unscaled by the corresponding eigenvalue. Several scaled time series are presented in Fig. S18. In addition, the right column (B, D, F, H, J) demonstrates that eigenvalues tend to be higher in the high latitudes, causing PCO1 for high-latitude sites to be upscaled, producing greater total spectral power in Fig. S9, relative to the low latitudes. Also for visual simplicity, we only present sites here that span the last 50,000 years; we direct readers to our Zenodo repository (*66*) where all data are present.

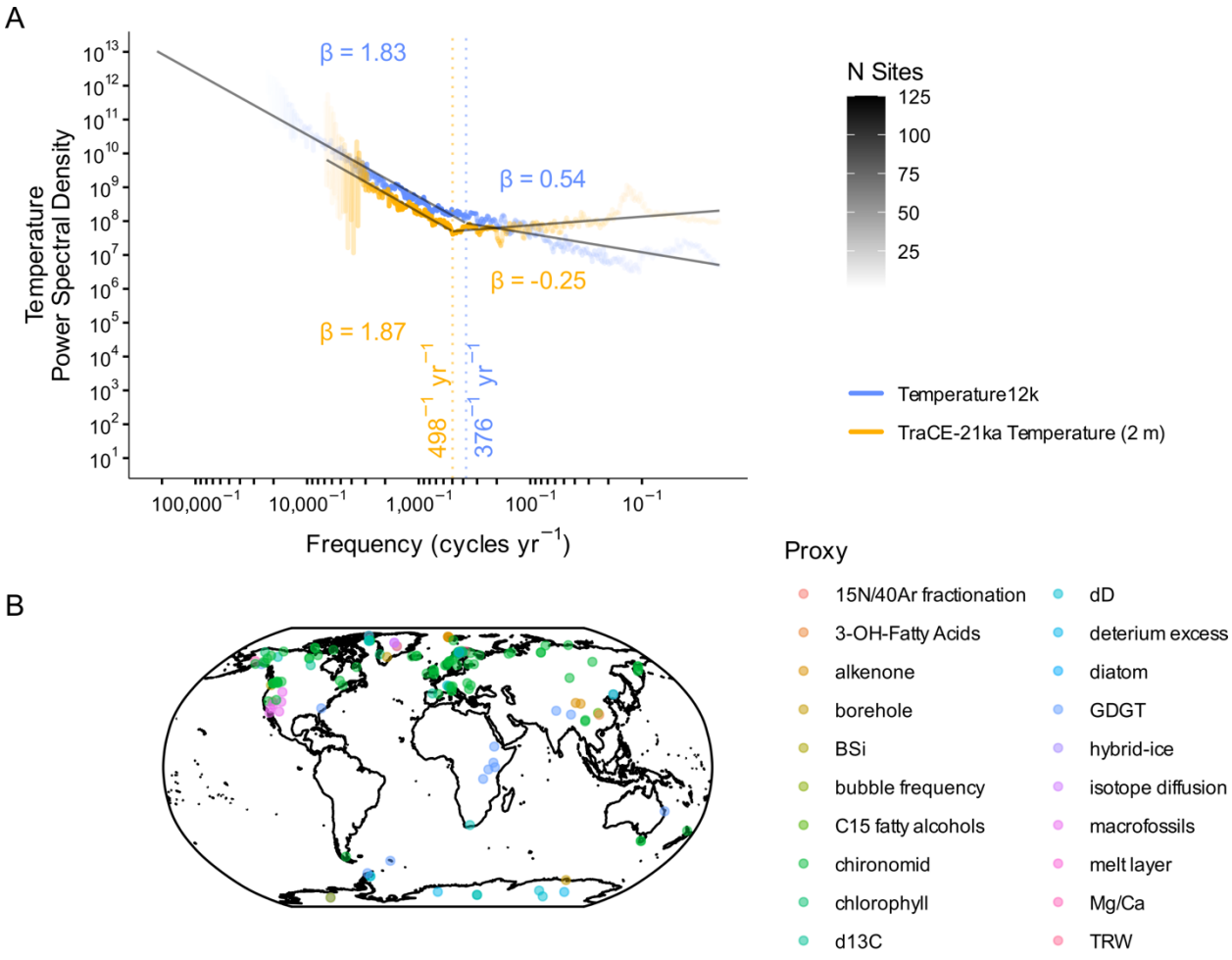

Fig. S3

(A) The averaged power spectrum for non-pollen temperature estimates from Temperature 12k (yellow). The averaged power spectrum of temperature variability for TraCE-21ka (blue) is estimated after degrading TraCE-21ka to match the time-averaged and spatial characteristics of the Temperature12k sites. Power spectra line opacity indicates the number of sites that resolve each frequency. Note the similar β at low frequencies and the similar break location between the high frequency and low frequency scaling regimes. (B) The Temperature12k sites are colored by proxy.

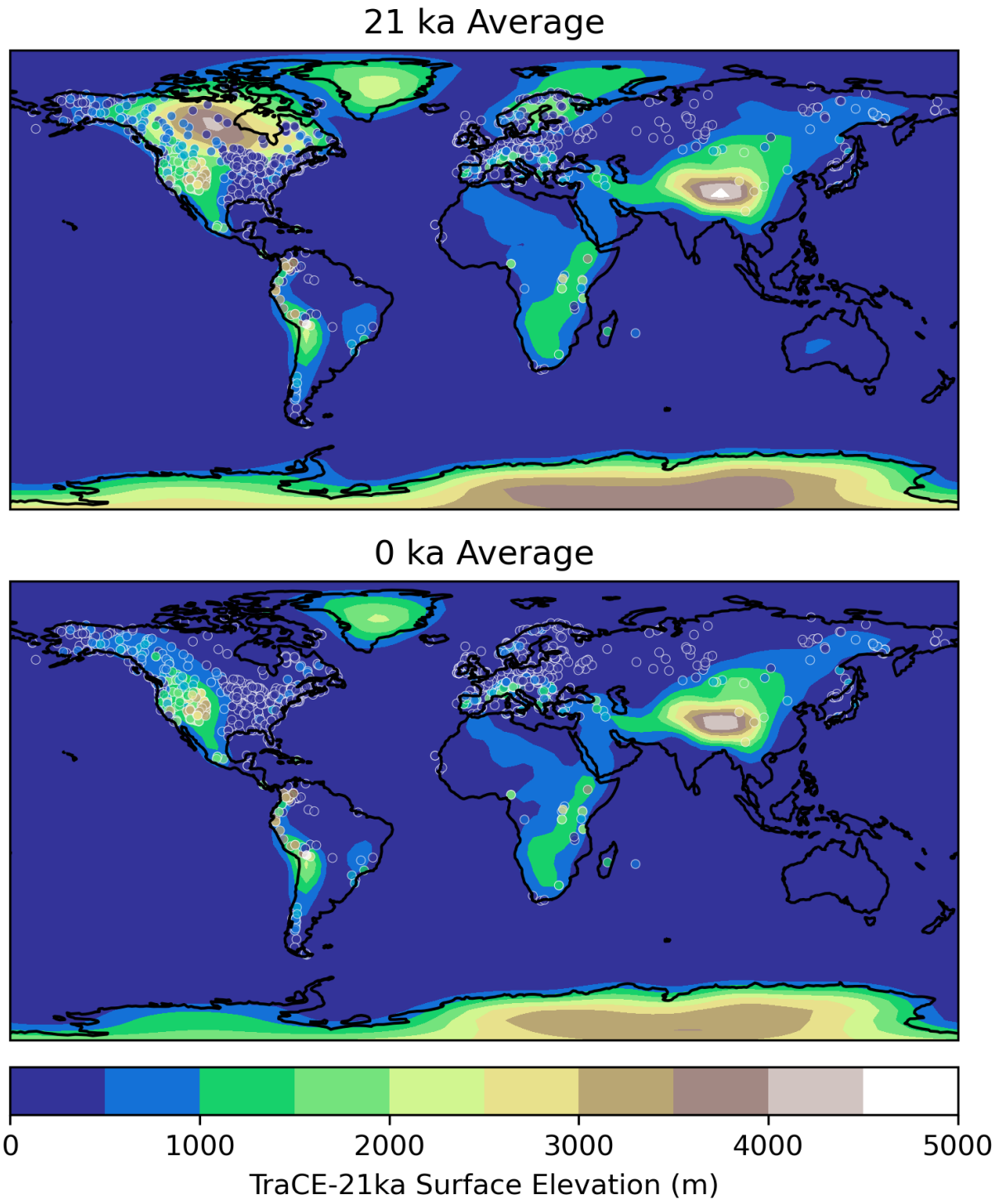

Fig. S4

Surface elevation for the TraCE-21ka simulations averaged for 21ka and 0ka, calculated using the surface geopotential (PHIS in CCSM3). The change in topography in North America and Antarctica from 21ka to 0ka is associated with a loss of the Laurentide Ice Sheet and a reduction

in ice volume in Antarctica. TraCE-21ka is simulated with ice sheet topography from the ICE-5G reconstruction (*100*)**.**

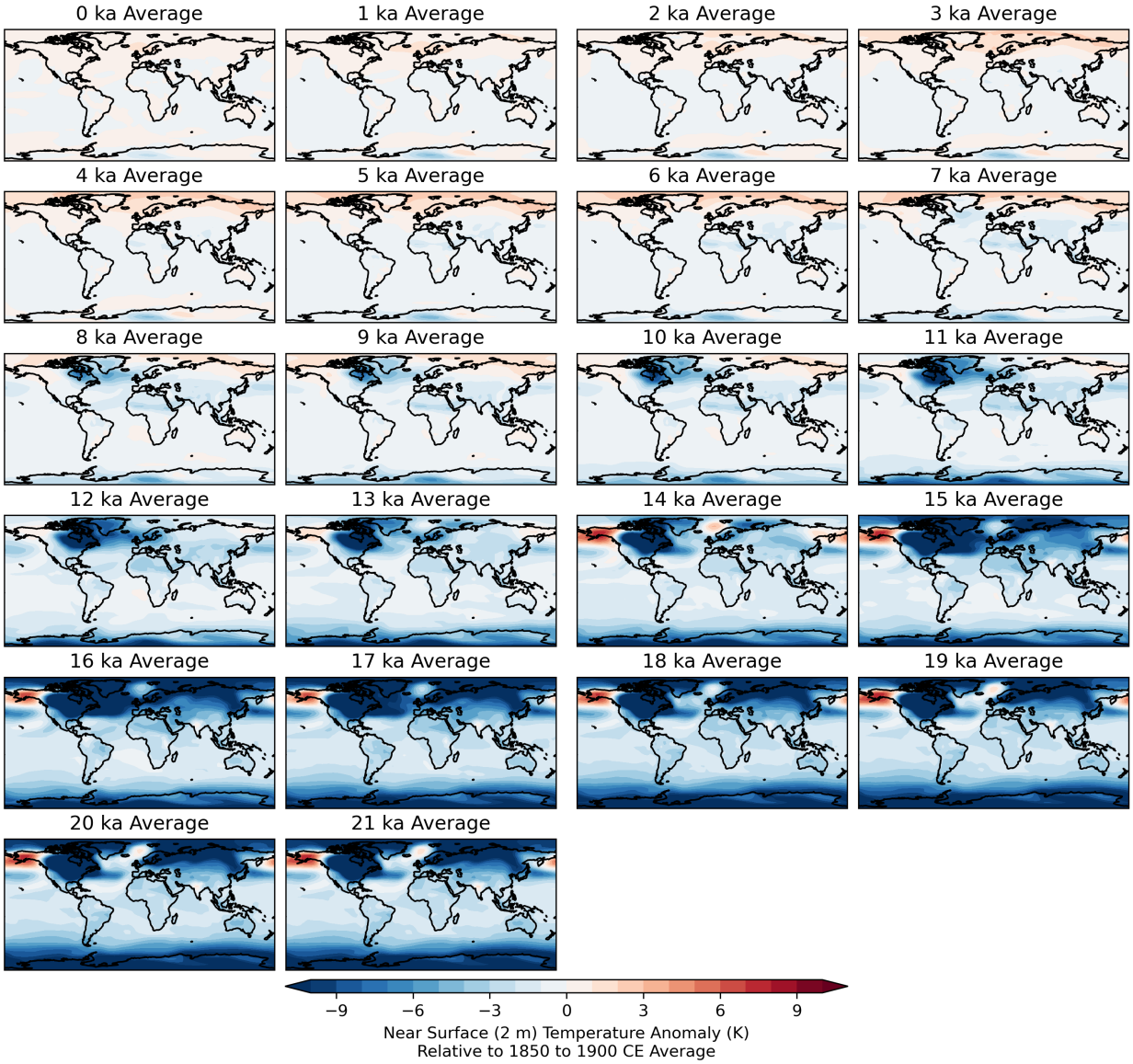

1438

1439 **Fig. S5**

1440 Near surface temperature anomalies for TraCE-21ka relative to an 1850 to 1900 CE baseline
1441 averaged every 1,000 years.
1442

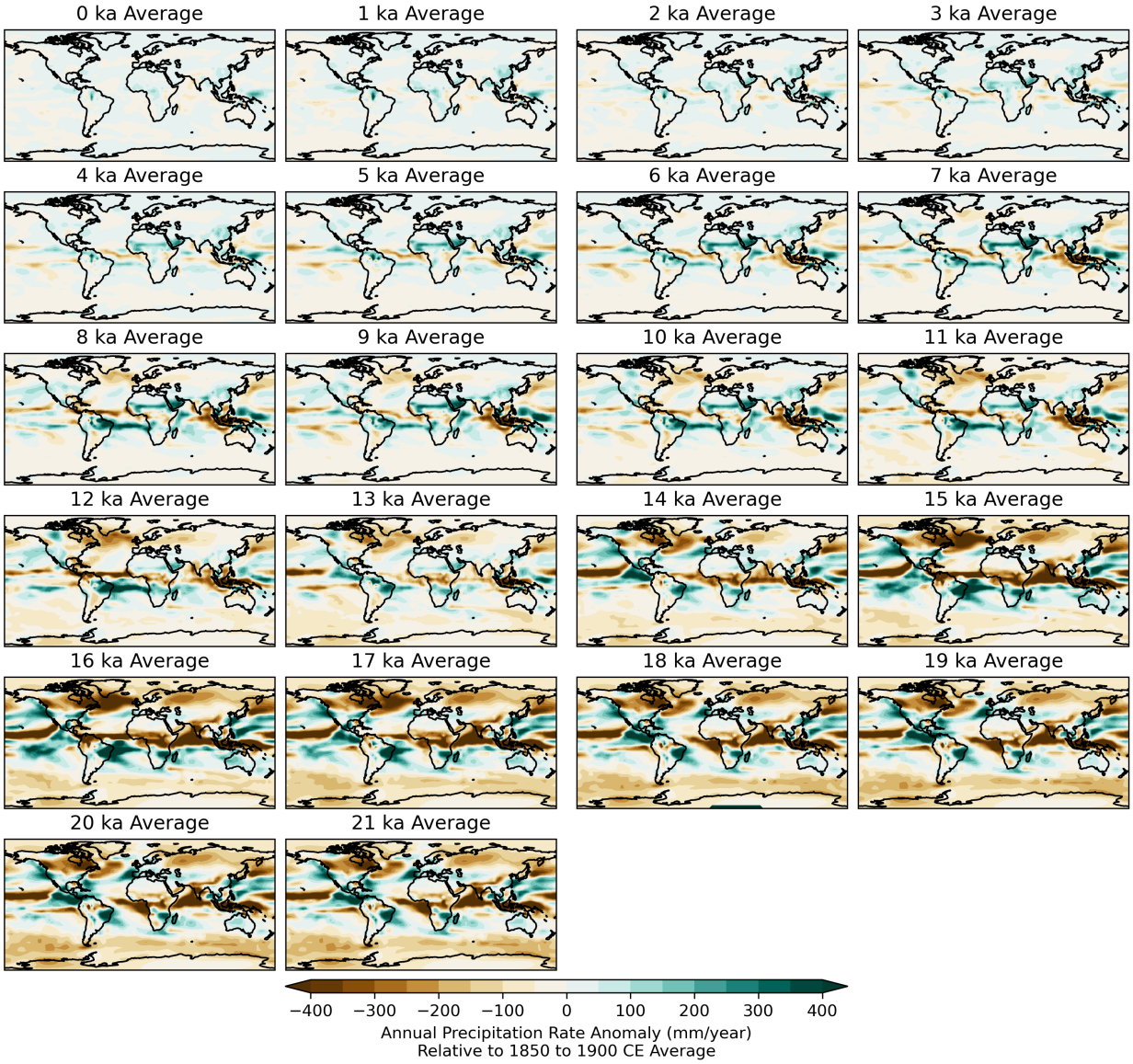

Fig. S6

As in Fig. S5 but for the total annual precipitation rate.

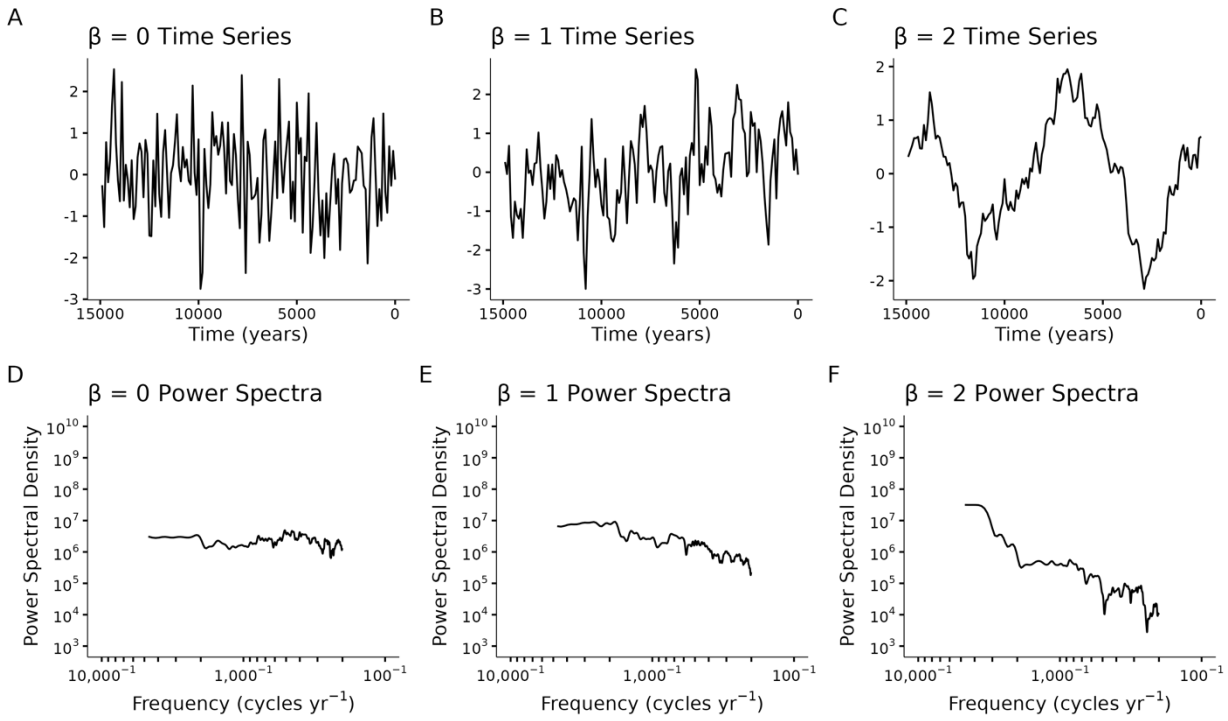

Fig. S7

(A-C) Synthetic time series with arbitrary units demonstrating a β of (A) 0, (B) 1, and (C) 2. (D-F) The corresponding power spectra for the synthetic time series in (A-C).

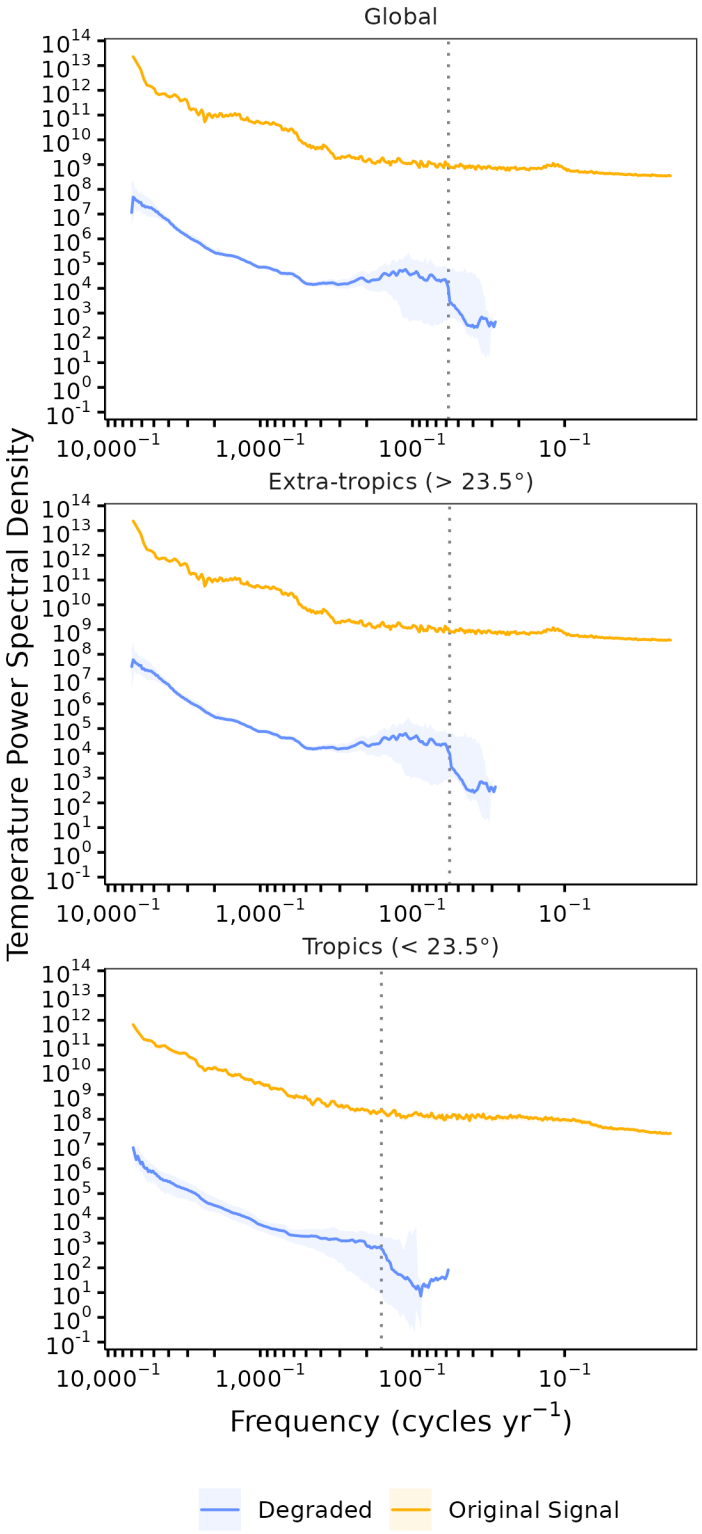
Global
Extra-tropics (> 23.5°)
Tropics (< 23.5°)
Temperature Power Spectral Density
Frequency (cycles yr^{-1})
10,000^{-1}
1,000^{-1}
100^{-1}
10^{-1}
Degraded
Original Signal

Fig. S8

Spectral power for near-surface temperature for TraCE-21ka at each fossil pollen site where the temperature time series is resolved annually (yellow) and degraded (blue) to match the temporal characteristics of the fossil pollen assemblage. For degradation, each annually-resolved temperature time series corresponding to the nearest grid cell to the fossil pollen site being analyzed was temporally subsampled to match the fossil pollen abundances and then smoothed using a low-pass filter with a timescale twice the mean resolution of the fossil pollen abundances (*33*). The frequency associated with a spurious drop in spectral power in the degraded power spectra, not present in the annually resolved power spectra, is defined as the highest resolvable frequency for (A) global, (B) extra-tropical, and (C) tropical spectral power estimates and marked with a dashed line. These frequencies are 58^{-1} $years^{-1}$, 57^{-1} $years^{-1}$, and 160^{-1} $years^{-1}$, respectively. Confidence intervals derive from the Monte-Carlo resampling procedure outlined in *Uncertainty Estimation.*

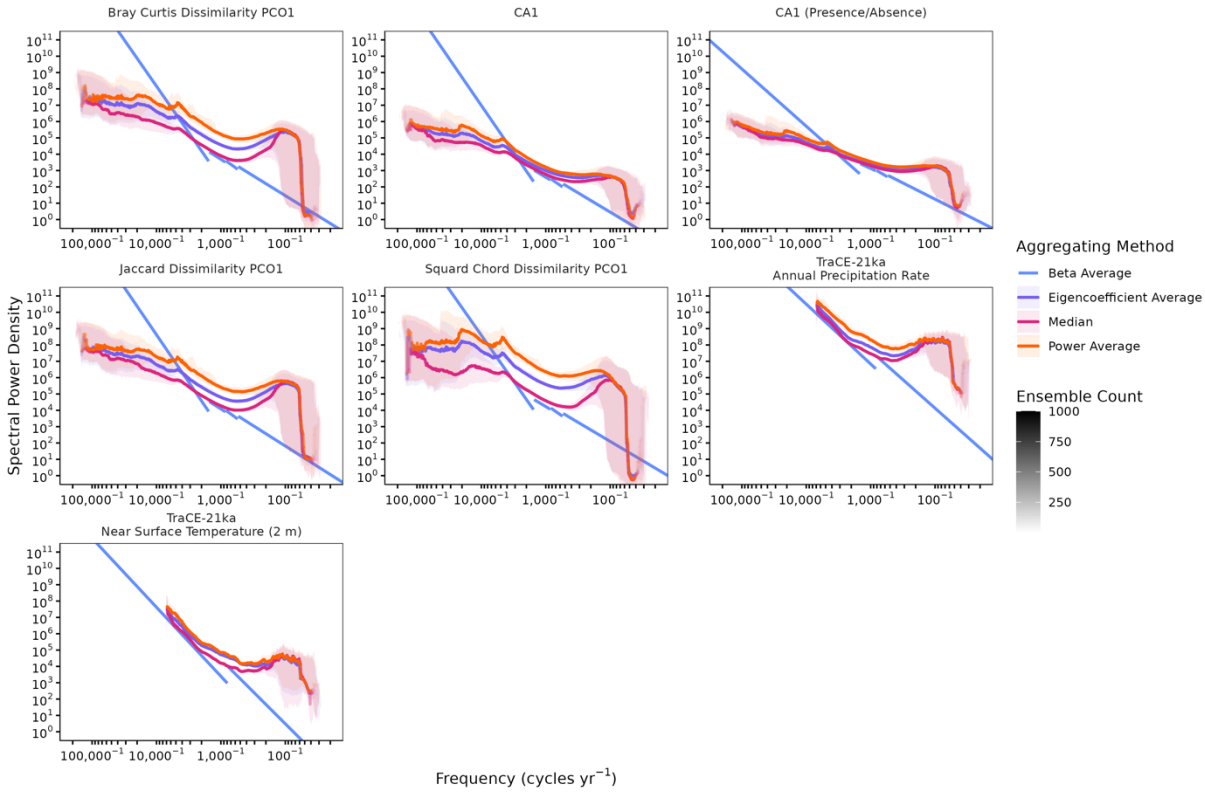

Fig. S9

Sensitivity tests for the continuum of ecological variability, in which the dimensionality-reduction methods and spectral-averaging methods are varied. Power spectra line opacity indicates the number of ensemble members that resolve each frequency. Results are presented for the primary dimension of variability from dimensionality reduction on fossil pollen assemblages. For the power average approach, we bin by frequency and then average the spectral power values across sites. For the eigencoefficient average approach, we bin by frequency and average the five MTM eigencoefficients corresponding to each data taper, across sites. We calculate spectral power following Equation 1. For the β average approach, we estimate β through an ordinary least squares regression between spectral power and frequency at a single site. We then average across sites to produce a global estimate of β. This procedure only retains β, not spectral power. Therefore, for the β average method only the resulting β fit is presented. The separate lines for β average correspond to β in four frequency bands. The breakpoint of these two lines indicates the calculated average break location averaged across sites. All sensitivity analyses were performed with the Monte Carlo resampling procedure detailed in *Uncertainty Estimation* with the shaded area corresponding to the 95% confidence interval. Note, that all averaged power spectra based on PCO1 (the first axis of Principal Coordinates Analysis) of the site-level community dissimilarity matrix demonstrate a decrease in β after the common ~17,000^{-1} years^{-1} breakpoint (β = 0.57 for Bray-Curtis PCO1, β = 0.72 for Jaccard PCO1, β = -0.08 for Squared Chord PCO1). This decrease is greatest in the squared chord dissimilarity metric which outperforms all other metrics for distinguishing modern fossil pollen assemblages that source from different ecosystems (i.e. is the most sensitive dissimilarity metric) (*63*, *64*). In contrast, CA1 (the first axis of Correspondence Analysis), which cannot saturate like metric-based approaches, shows no

such decrease in β. The averaged power spectra for CA1, which represents the primary dimension of variation in fossil pollen assemblages (not the dissimilarity matrix), has a higher β (β = 0.87 for frequencies lower than the $18{,}395^{-1}$ $years^{-1}$ breakpoint) and more consistent βs across all frequencies, demonstrating that the decrease in β observed at low frequencies for PCO-based approaches is caused by metric saturation.

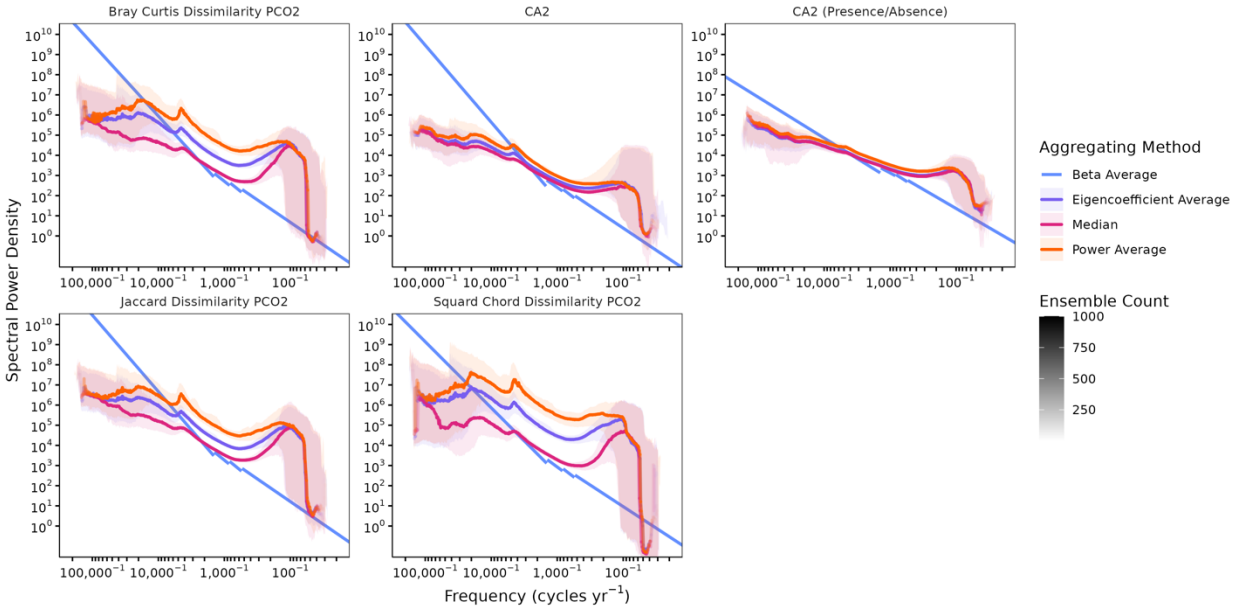

Fig. S10

As in Fig. S9, for the secondary dimension of variability from dimensionality reduction on fossil pollen assemblages.

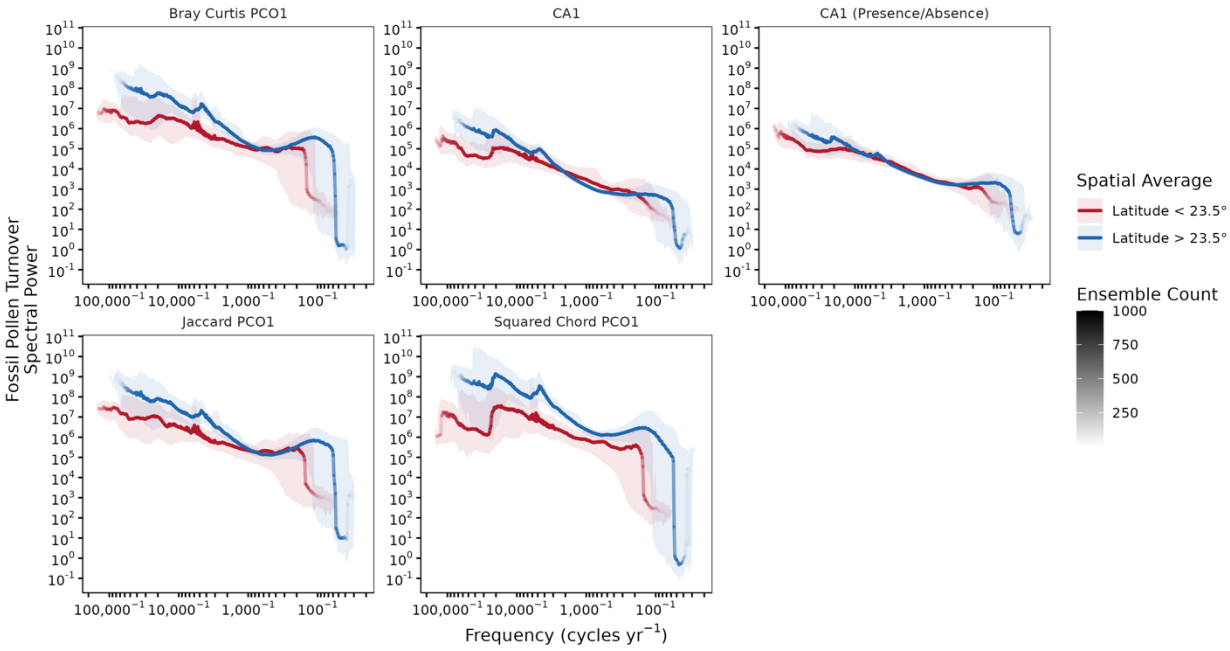

Fig. S11

Sensitivity tests for latitudinal averaged power spectra for PCO1 of fossil pollen assemblages where the dimensionality reduction method is varied. All power spectra were generated by averaging spectral power after binning by frequency. Power spectra line opacity indicates the number of ensemble members that resolve each frequency.

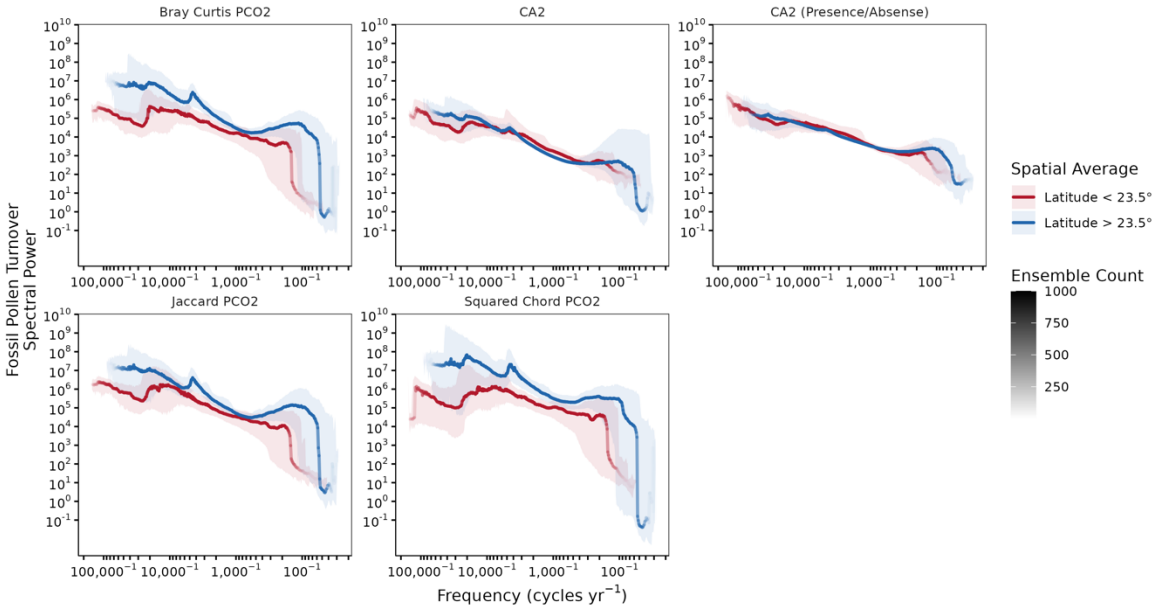

Fig. S12

As in Fig. S11 but for PCO2 from fossil pollen assemblages.

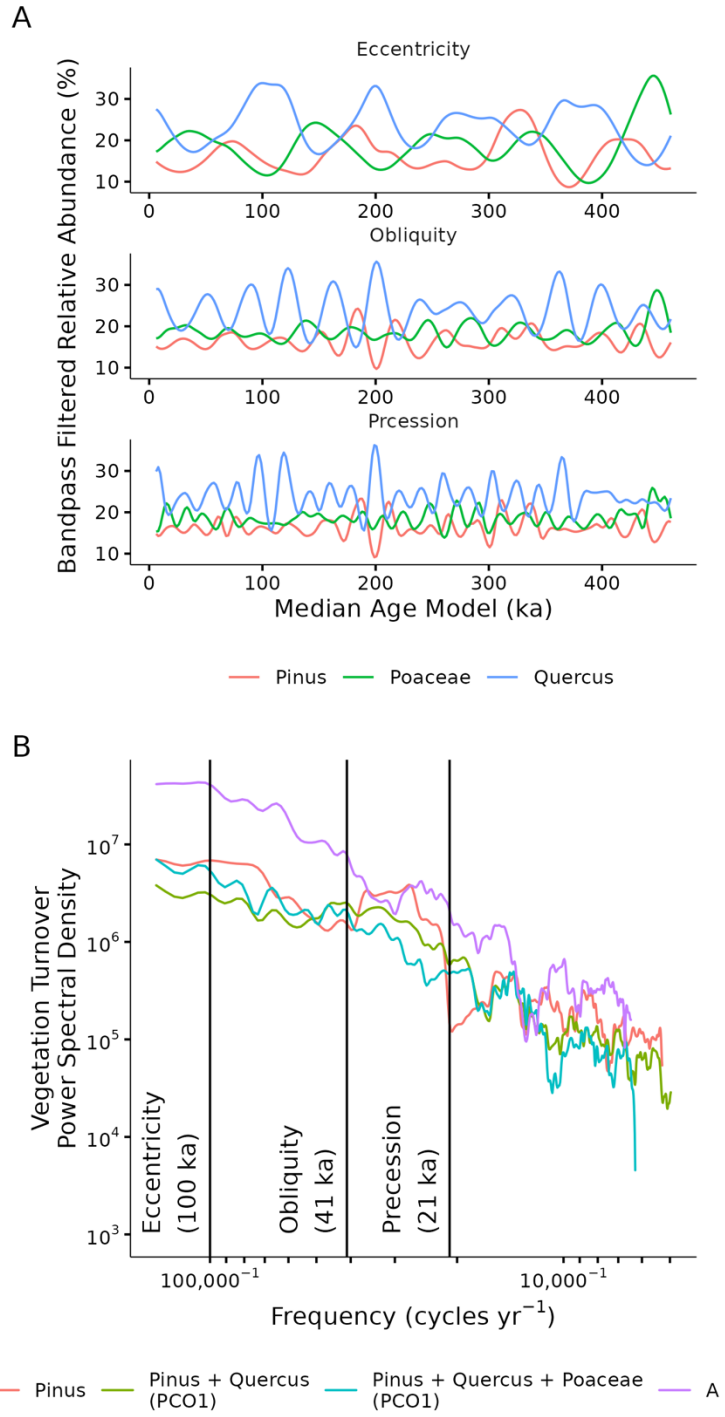

Fig. S13

(A) Taner filtered relative abundance of the three most abundant taxa at Ioannina (Dataset ID: 4112) for the precession (21,000 year), obliquity (41,000), and eccentricity (100,000 year) Milankovitch cycles: *Pinus* (red), *Quercus* (blue), and Poaceae (green). A filter window from 25,000^{-1} to 18,000^{-1} years^{-1} was used to isolate the precession signal. A filter window from 45,000^{-1} to 35,000^{-1} years^{-1} was used to isolate the obliquity signal. A filter window from

1522 $120{,}000^{-1}$ to $80{,}000^{-1}$ $years^{-1}$ was used to isolate the eccentricity signal. Note, that *Pinus*,
1523 Poaceae, and *Quercus* are out of phase for each Milankovitch cycle. (B) The effect of these out
1524 of phase relative abundance changes on periodic signals in the relative abundance and primary
1525 dimension of variability at site Ioannina. The red line corresponds to MTM performed on *Pinus*
1526 pollen relative abundance, not the primary mode of variability from PCO since more than one
1527 taxa is needed to generate a dissimilarity matrix. The green line corresponds to MTM performed
1528 on the primary dimension of variability of the dissimilarity matrix calculated with *Pinus* and
1529 *Quercus* relative abundances. For the blue line, Poaceae was added when calculating the
1530 dissimilarity matrix. In all instances, the out of phase behavior in (A) causes the periodic signal
1531 present in *Pinus* relative abundance near the obliquity band to diminish. MTM on PCO1 of the
1532 dissimilarity matrix of all taxa at Ioannina corresponds to the purple line.
1533

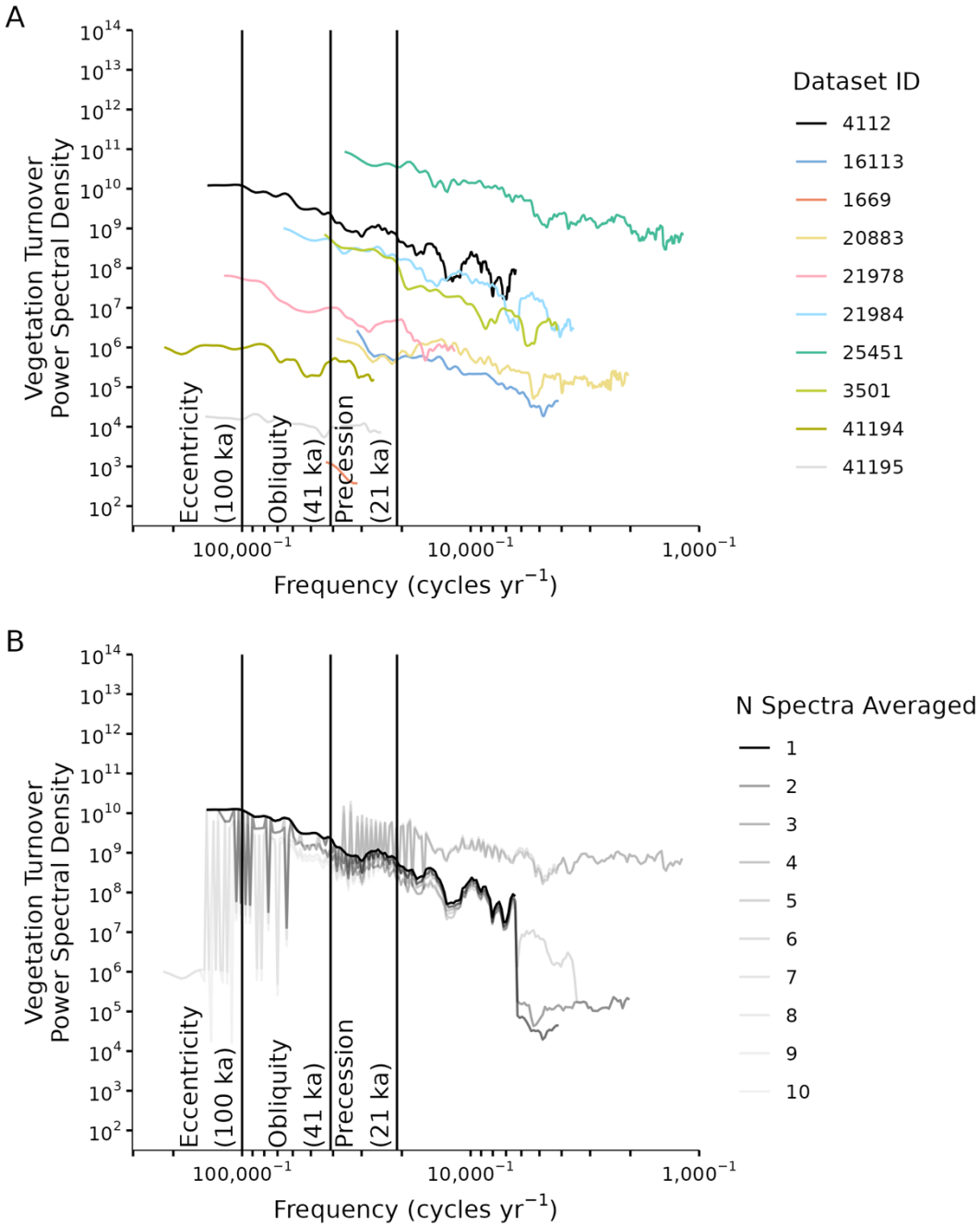

Fig. S14

(A) Spectral power from the ten longest records from our Neotoma compilation. High spectral power at all Milankovitch bands is particularly well expressed at ODP Site 658 (41194) and Páramo de Agua Blanca (21978). (B) The effect of averaging spectral power across these sites, each with a unique sampling resolution and temporal span. Here, the averaging is a running mean from the site order in A. For instance, "N Spectra Averaged" of one is the Ioannina (4112) record; a value of two is the average of Ioannina (4112) and Grays Lake (16113); a value of three is the average of Ioannina (4112), Grays Lake (16113), and Lake Louise (1669). We use the

median Bchron age model in these analyses and do not employ the resampling procedure of the main manuscript.

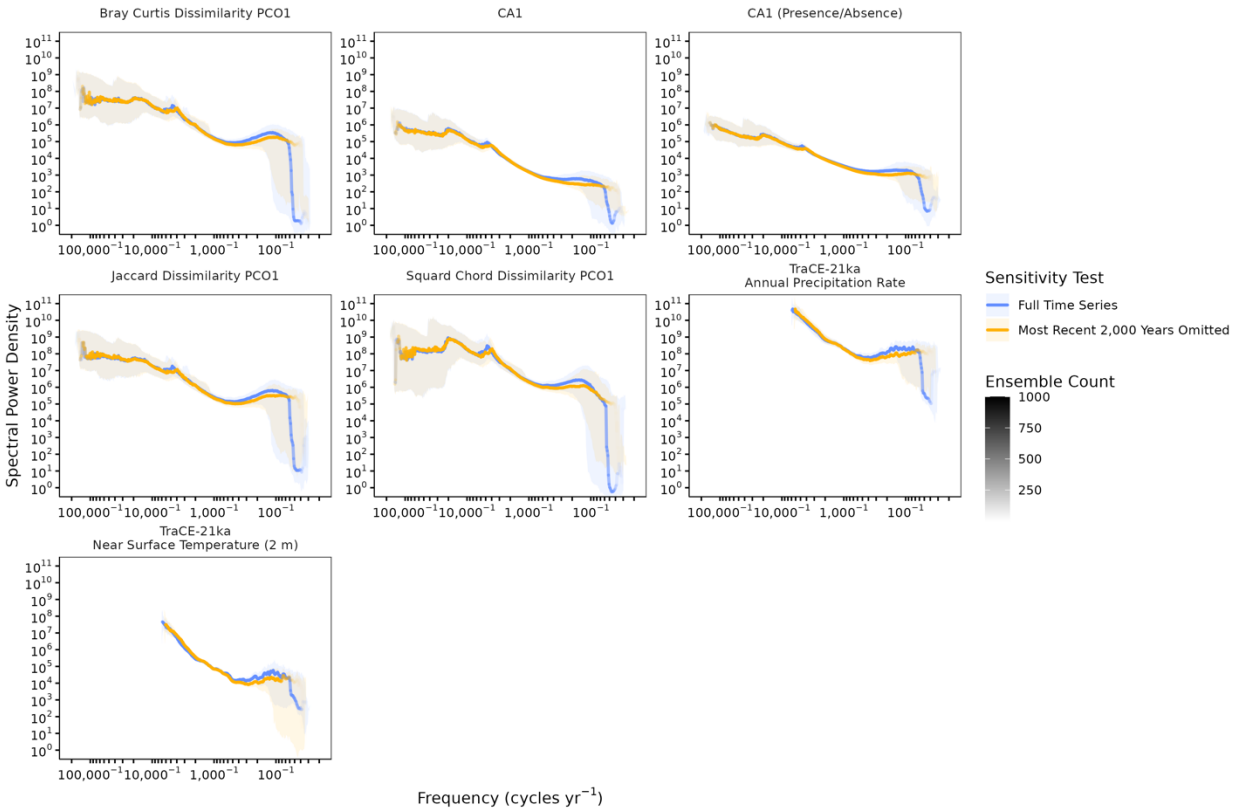

Fig. S15

Sensitivity tests for the continuum of vegetation turnover and climate variability based on the median of an ensemble of spectral power estimates after removing any observations younger than 2,000 years, to assess the influence of anthropogenic land use change. The blue line corresponds to results from Fig. 2 and Fig. S9 and the yellow line corresponds to the sensitivity test. Power spectra line opacity indicates the number of ensemble members that resolve each frequency. Note, that the confidence intervals for the power spectra overlap across all of frequency space suggesting a limited influence of anthropogenic land use change.

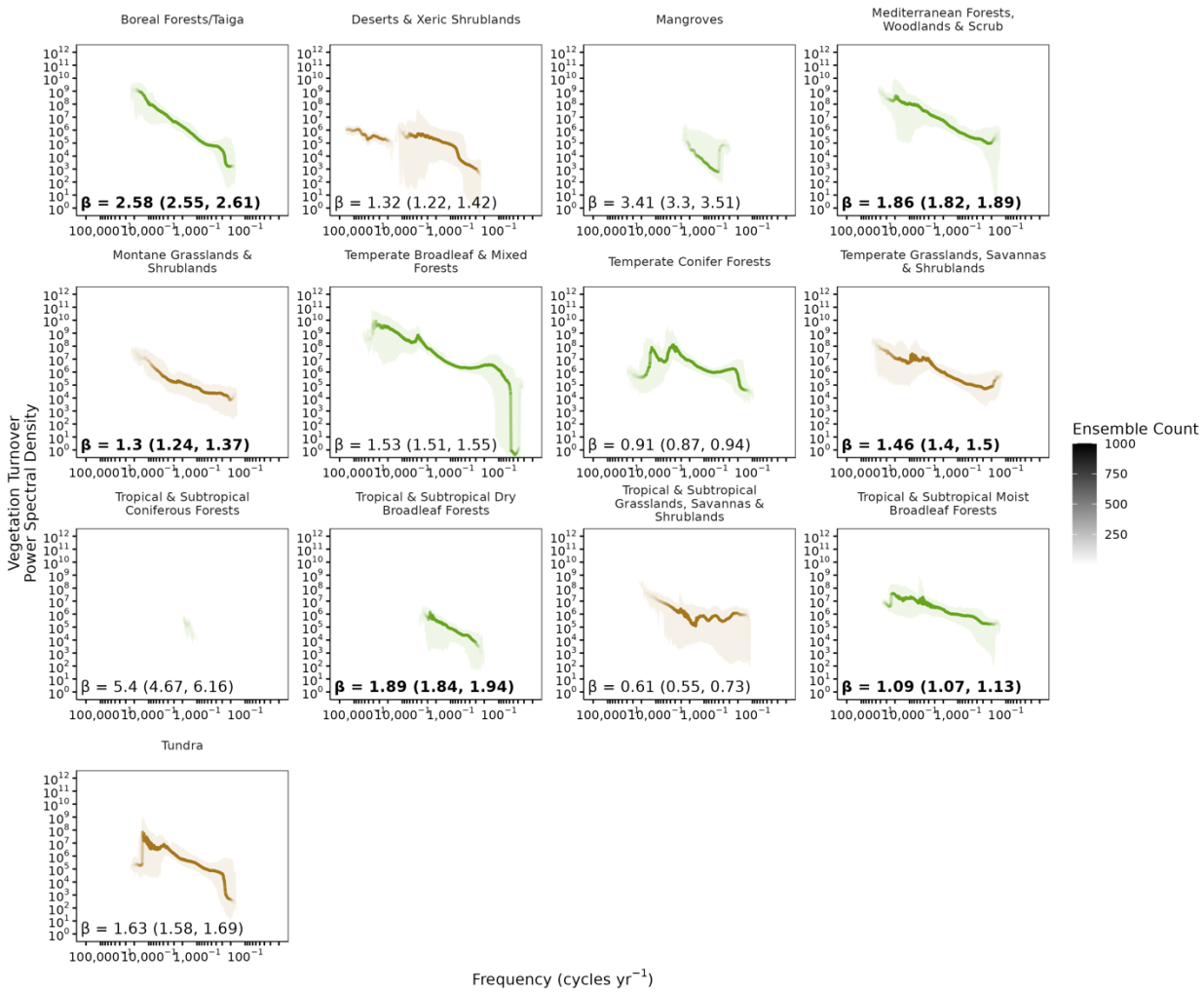

Fig. S16

Power spectra for vegetation turnover averaged across biomes, unlike the global, tropical, and extra-tropical averages in Fig. 2 and Fig. 3. Line coloring corresponds to biomes that have a large proportion of grasses (brown) or a large proportion of trees (green). β was estimated across each, entire power spectra (i.e. no breakpoint identification) and the bold text corresponds to power spectra where a single β estimate fits the power-law scaling relationship between spectral power and frequency well. For instance, vegetation turnover in the Tropical & Subtropical Grasslands, Savannas & Shrublands biomes have two scaling regimes. Frequencies lower than ~2,000^{-1} years^{-1} have a large increase in spectral power with decreasing frequency. In contrast, frequencies higher than ~2,000^{-1} years^{-1} have uniform spectral power. For this reason, a single β value poorly represents the non-linear scaling relationship. Note, that the gap in the power spectrum of Deserts & Xeric Shrublands is caused by the power spectra of two long records at coarse resolution (ODP658, Dataset ID: 41194, 41195, off the western coast of the Sahara Desert in Fig. S17, Data S1) being averaged with short, comparatively high resolution records. A lack of sites with intermediate resolution and temporal span in the Deserts & Xeric Shrubland biome causes a gap spectral power when all sites in the biome are averaged together.

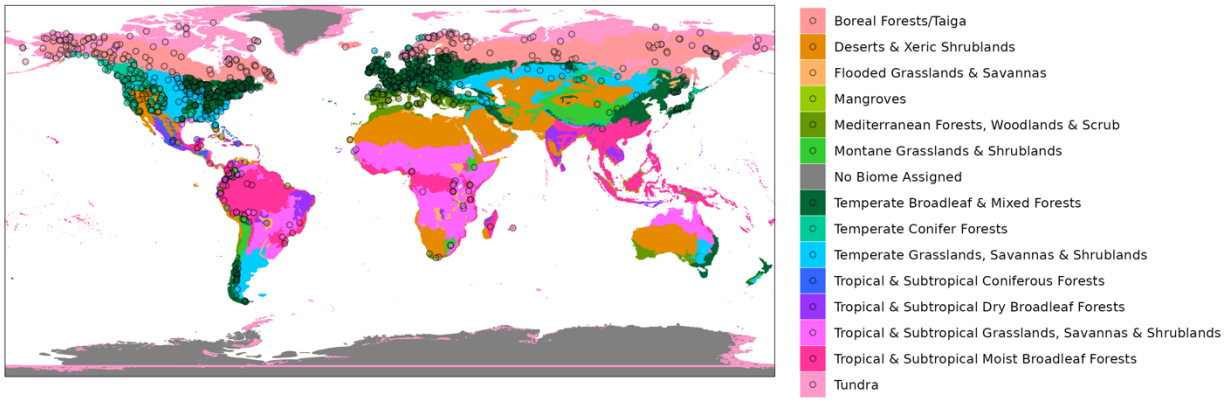

Fig. S17

Biome classifications for each site in our compilation based on ecoregions determined by Dinerstein et al (*99*).

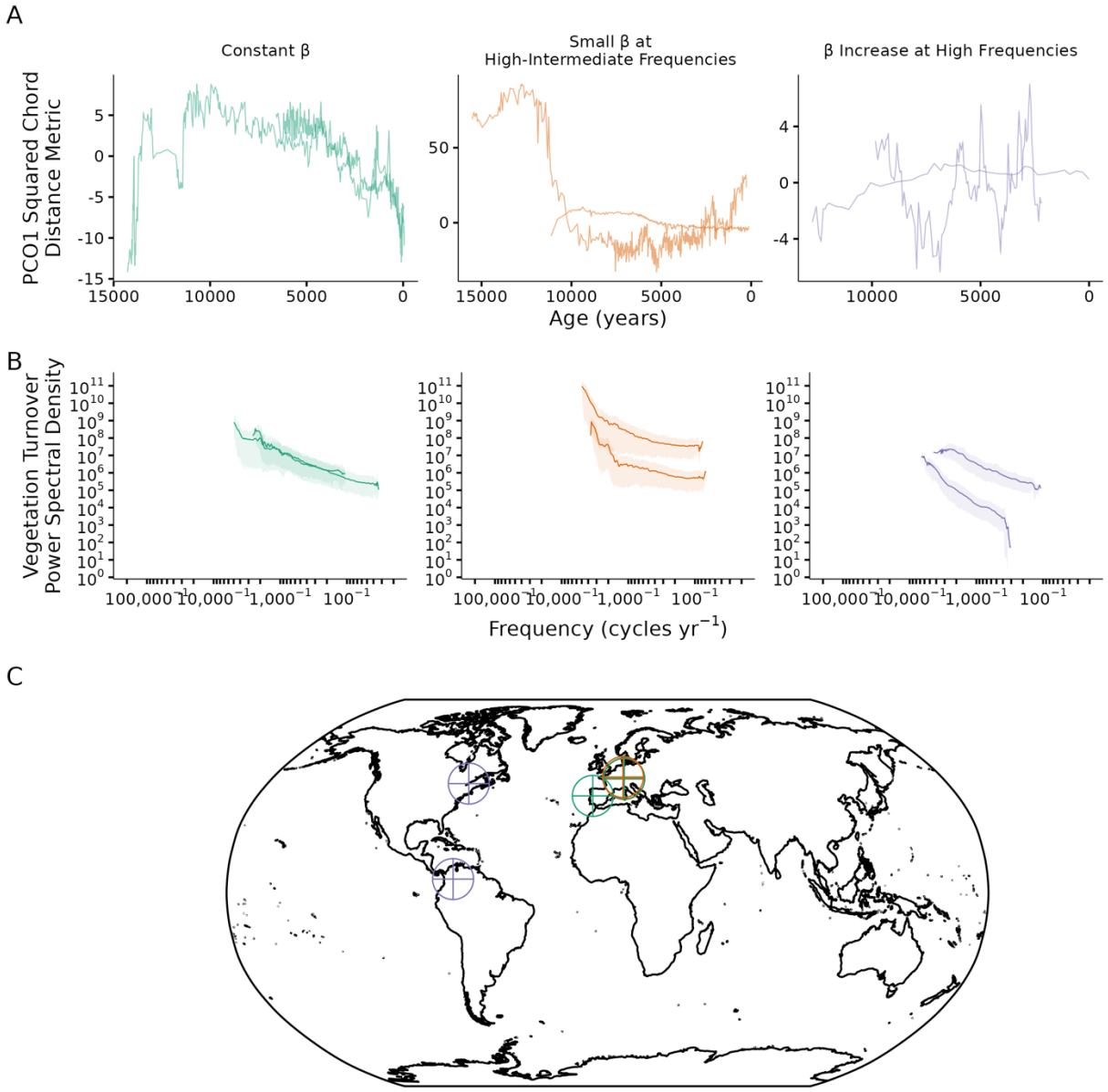

Fig. S18

(A) Individual records of vegetation turnover from the 1,321 site compilation that are selected to demonstrate characteristics of the global average power spectra that are presented in Fig. 2 and Fig. 3. Sites that demonstrate a constant β at millennial frequencies are colored in green and correspond to the globally averaged spectrum of vegetation turnover from 797^{-1} to $18{,}012^{-1}$ years^{-1} (Dataset IDs: 40999, 41909). Sites that have a low β at high-intermediate frequencies are colored in orange and correspond to the globally averaged spectrum of vegetation turnover from 149^{-1} to 797^{-1} years^{-1} (Dataset IDs: 40958, 42692). Sites that demonstrate a high β at the highest frequencies are colored in purple and correspond to the globally averaged spectrum of vegetation turnover for frequencies higher than 149^{-1} years^{-1} (Dataset IDs: 219, 21702). (B) The power

spectra for the vegetation turnover time series in (A). (C) The location of sites presented in (A). The colors correspond to different spectral characteristics that are highlighted in the main text. Note, that all sites demonstrate a decrease in β at multimillennial timescales present in the global average at frequencies lower than $18{,}012^{-1}$ $years^{-1}$. Note, in (A) the PCO1 time series are scaled by the corresponding eigenvalue, unlike in Fig. S2.

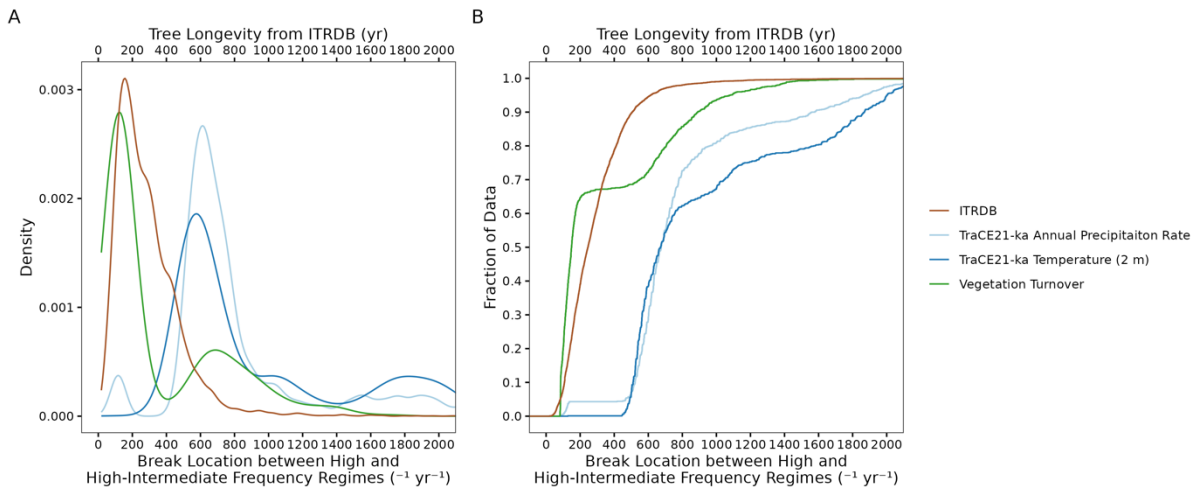

Fig. S19

(A) Probability density distributions and (B) empirical cumulative distributions for the ensemble of breakpoints estimated for globally averaged power spectra between the low-intermediate and high-intermediate frequency band for fossil pollen (green) from our Monte Carlo resampling approach, compared to tree longevity estimates from the International Tree Ring Data Bank (brown). Break locations for TraCE-21ka near-surface temperature (blue) and TraCE-21ka precipitation (light blue) correspond to one break location, previously reported (*5*, *6*), at frequencies between 100^{-1} to 1,000 $years^{-1}$. Tree longevity from the International Tree Ring Data Bank corresponds to the top horizontal axis. All pollen results presented are from PCO1 using the squared chord distance metric and averaged by spectral power.

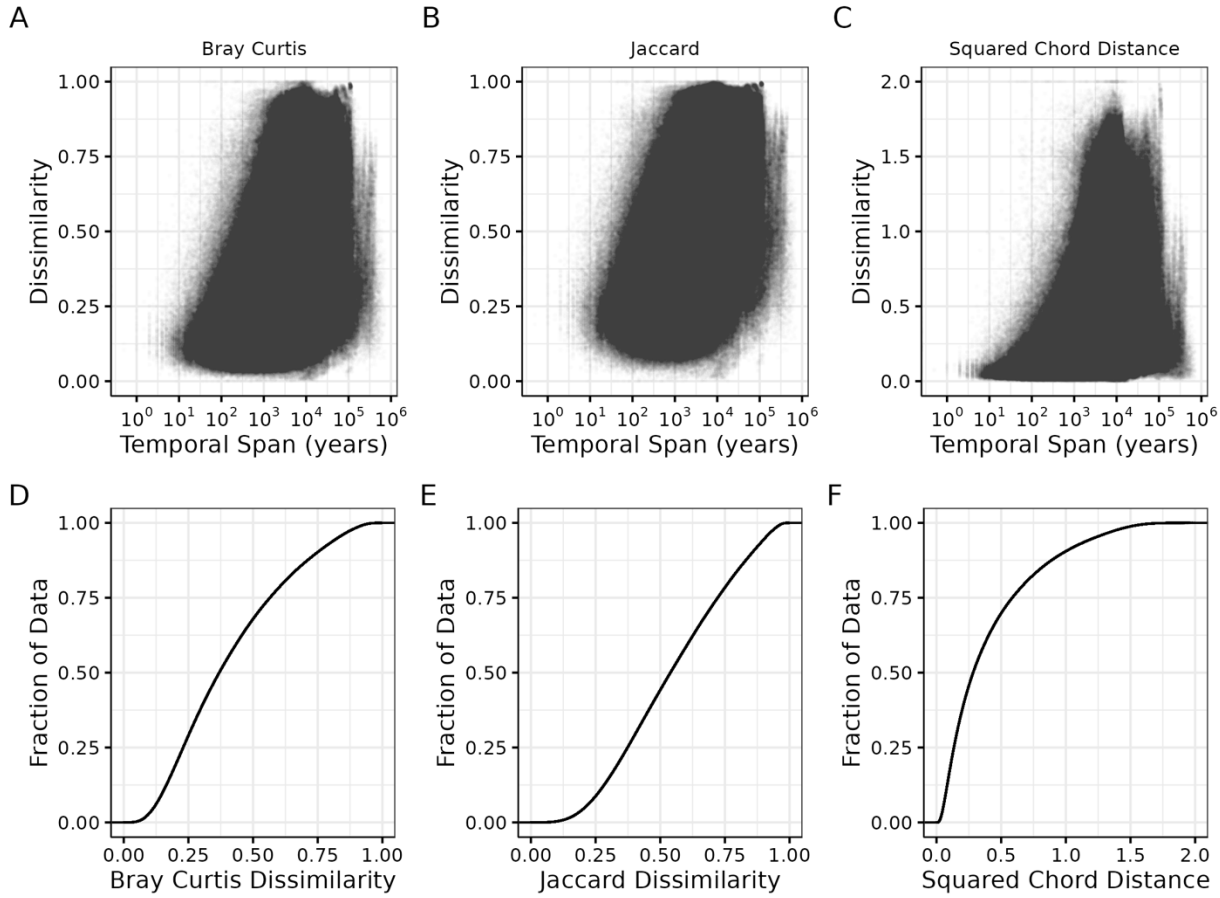

Fig. S20

(A-C) Measured vegetation assemblage dissimilarity, for all sites in the global fossil pollen compilation. Dissimilarity was calculated only for assemblages from the same site and was not calculated for assemblages from different sites. Within each site, all possible pairs of fossil pollen assemblages were compared using the (A) Bray Curtis, (B) Jaccard, and (C) Squared Chord Distance metrics with the corresponding temporal span between the samples being compared retained. (D-F) The empirical cumulative distribution of all points shown in the top row of plots.


Fossil Pollen
β High Frequency Regime
Fossil Pollen
β High-Intermediate Frequency Regime
Fossil Pollen
β Low Frequency Regime
Fossil Pollen
β Low-Intermediate Frequency Regime
Fossil Pollen log10(High Frequency Regime - High-Intermediate Frequency Regime Break Location)
Fossil Pollen log10(High-Intermediate Frequency Regime - Low-Intermediate Frequency Regime Break Location)
Fossil Pollen log10(Low-Intermediate Frequency Regime - Low Frequency Regime Break Location)
Precipitation
β High Frequency Regime
Precipitation
β Low Frequency Regime
Precipitation log10(High Frequency Regime - Low Frequency Regime Break Location)
Temperature
β High Frequency Regime
Temperature
β Low Frequency Regime
Temperature log10(High Frequency Regime - Low Frequency Regime Break Location)
Density
Parameter
Fossil Pollen
TraCE-21ka Annual Precipitation Rate
TraCE-21ka Near Surface Temperature (2 m)

Fig. S21

Each plot corresponds to the probability density function for all breakpoint and β parameter estimates in Fig. 2 and Table S1. Colors correspond to parameter estimates for fossil pollen (green), TraCE-21ka annual precipitation rate (light blue), and TraCE-21ka near-surface temperature (blue).

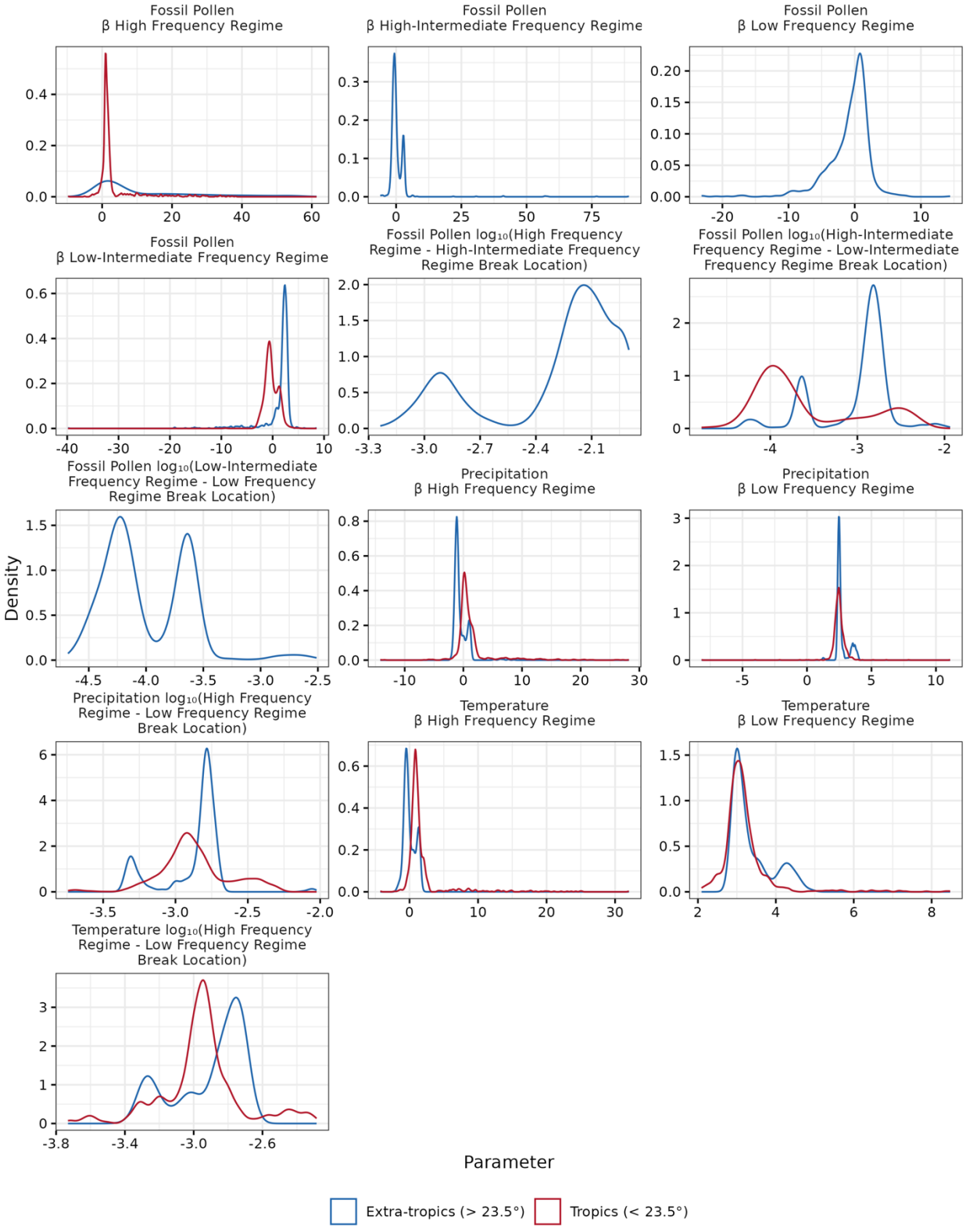
Fossil Pollen
β High Frequency Regime
Fossil Pollen
β High-Intermediate Frequency Regime
Fossil Pollen
β Low Frequency Regime
Fossil Pollen
β Low-Intermediate Frequency Regime
Fossil Pollen log10(High Frequency Regime - High-Intermediate Frequency Regime Break Location)
Fossil Pollen log10(High-Intermediate Frequency Regime - Low-Intermediate Frequency Regime Break Location)
Fossil Pollen log10(Low-Intermediate Frequency Regime - Low Frequency Regime Break Location)
Precipitation
β High Frequency Regime
Precipitation
β Low Frequency Regime
Precipitation log10(High Frequency Regime - Low Frequency Regime Break Location)
Temperature
β High Frequency Regime
Temperature
β Low Frequency Regime
Temperature log10(High Frequency Regime - Low Frequency Regime Break Location)
Density
Parameter
Extra-tropics (> 23.5°)
Tropics (< 23.5°)

Fig. S22

As in Fig. S21 but for breakpoint and β estimates in Fig. 3. Colors correspond to the spatial average with red indicating the tropics (< 23.5°) and blue indicating the extra-tropics (> 23.5°).

1635

Vegetation

	β					Breakpoint	
	High Frequency Band	High-Intermediate Frequency Band	Low-Intermediate Frequency Band	Low Frequency Band	High Frequency Band - High-Intermediate Frequency Band ($^{-1}$ years^{-1})	High-Intermediate Frequency Band - Low-Intermediate Frequency Band ($^{-1}$ years^{-1})	Low-Intermediate Frequency Band – Low Frequency Band ($^{-1}$ years^{-1})
Global	4.34*† (3.64, 4.96)	0.35*† (0.02, 0.83)	1.78*† (1.67, 1.87)	-0.08† (-0.23, -0.06)	149* (154, 145)	797* (862, 797)	18,012* (18,952, 17,254)
Extra-tropics (> 23.5°)	4.34*† (3.79, 4.93)	-0.36*† (-0.43, -0.28)	2.20*† (2.16, 2.26)	-0.05† (-0.24, 0.11)	148* (153, 142)	712* (730, 698)	13,885* (14,495, 13,160)
Tropics (< 23.5°)	1.30*† (1.21, 1.38)			-0.43*† (-0.51, -0.38)			6,877* (7,499, 6,383)

1636

TraCE-21ka near-surface Temperature (2 m)

	β		Breakpoint
	High Frequency Band	Low Frequency Band (Climate Regime)	High Frequency Band - Low Frequency Band. ($^{-1}$ years^{-1})
Global	-0.24*† (-0.29, -0.18)	3.10*† (3.07, 3.13)	672* (693, 649)
Extra-tropics (> 23.5°)	-0.26*† (-0.30, -0.21)	3.14*† (3.11, 3.17)	674* (691, 649)
Tropics (< 23.5°)	0.94*† (0.91, 1.00)	3.08*† (3.06, 3.10)	894* (909, 886)

1637

TraCE-21ka Annual Precipitation Rate

		B	Breakpoint
	High Frequency Band	Low Frequency Band (Climate Regime)	High Frequency Band - Low Frequency Band ($^{-1}$ years^{-1})
Global	-0.53*† (-0.58, -0.49)	2.696*† (2.68, 2.705)	676* (691, 660)
Extra-tropics (> 23.5°)	-0.99*† (-1.01, -0.96)	2.52*† (2.51, 2.53)	628* (632, 618)
Tropics (< 23.5°)	0.47*† (0.41, 0.53)	2.47*† (2.45, 2.48)	795* (814, 776)

Table S1

Parameter estimates and corresponding 95% confidence intervals (in parentheses) for Fig. 2 and Fig. 3. * indicates that the estimated parameter is statistically distinct from 0 based on the bootstrapped confidence interval. For estimates of β, † indicates that β is statistically distinct from 2 (i.e. red noise) based on the bootstrapped confidence interval (for methods, see section *Statistical Comparisons between Estimated Parameters from Spectral Analyses*).

	Vegetation Turnover High Frequency Band - High-Intermediate Frequency Band Break Location	Vegetation Turnover High-Intermediate Frequency Band - Low-Intermediate Frequency Band Break Location	Vegetation Turnover Low-Intermediate Frequency Band - Low Frequency Band Break Location	TraCE-21ka Temperature High Frequency Band - Low Frequency Band Break Location	TraCE-21ka Annual Precipitation Rate High Frequency Band - Low Frequency Band Break Location
Vegetation Turnover High Frequency Band - High-Intermediate Frequency Band Break Location					
Vegetation Turnover High-Intermediate Frequency Band - Low-Intermediate Frequency Band Break Location	< 0.001***				
Vegetation Turnover Low-Intermediate Frequency Band - Low Frequency Band Break Location	< 0.001***	< 0.001***			
TraCE-21ka Temperature High Frequency Band - Low Frequency Band Break Location	< 0.001***	< 0.001***	< 0.001***		
TraCE-21ka Annual Precipitation Rate High Frequency Band - Low Frequency Band Break Location	< 0.001***	< 0.001***	< 0.001***	0.693	

Table S2

P-values of permutation tests comparing break locations from Fig. 2 where *** corresponds to values <0.001, ** indicates values between 0.001 and 0.01, and * indicates values between 0.01 and 0.05.

	Vegetation Turnover β High Frequency Band	Vegetation Turnover β High-Intermediate Frequency Band	Vegetation Turnover β Low-Intermediate Frequency Band	Vegetation Turnover β Low Frequency Band	TraCE-21ka Temperature β High Frequency Band	TraCE-21ka Temperature β Low Frequency Band	TraCE-21ka Annual Precipitation Rate β High Frequency Band	TraCE-21ka Annual Precipitation Rate β Low Frequency Band
Vegetation Turnover β High Frequency Band								
Vegetation Turnover β High-Intermediate Frequency Band	< 0.001***							
Vegetation Turnover β Low-Intermediate Frequency Band	< 0.001***	< 0.001***						
Vegetation Turnover β Low Frequency Band	< 0.001***	0.0543	< 0.001***					
TraCE-21ka Temperature β High Frequency Band	< 0.001***	< 0.001***	< 0.001***	0.0171 **				
TraCE-21ka Temperature β Low Frequency Band	< 0.001***	< 0.001***	< 0.001***	< 0.001**	< 0.001***			
TraCE-21ka Annual Precipitation Rate β High Frequency Band	< 0.001***	< 0.001***	< 0.001***	< 0.001**	< 0.001***	< 0.001***		
TraCE-21ka Annual Precipitation Rate β Low Frequency Band	< 0.001***	< 0.001***	< 0.001***	< 0.001**	< 0.001***	< 0.001***	< 0.001***	

Table S3

P-values of permutation tests comparing β from Fig. 2 where *** corresponds to values <0.001, ** indicates values between 0.001 and 0.01, and * indicates values between 0.01 and 0.05.

	Latitude > 23.5° Vegetation Turnover β High Frequency Band	Latitude > 23.5° Vegetation Turnover β High-Intermediate Frequency Band	Latitude > 23.5° Vegetation Turnover β Low-Intermediate Frequency Band	Latitude > 23.5° Vegetation Turnover β Low Frequency Band	Latitude > 23.5° TraCE-21ka Temperature β High Frequency Band	Latitude > 23.5° TraCE-21ka Temperature β Low Frequency Band	Latitude > 23.5° TraCE-21ka Annual Precipitation Rate β High Frequency Band	Latitude > 23.5° TraCE-21ka Annual Precipitation Rate β Low Frequency Band
Latitude > 23.5° Vegetation Turnover β High Frequency Band								
Latitude > 23.5° Vegetation Turnover β High-Intermediate Frequency Band	< 0.001***							
Latitude > 23.5° Vegetation Turnover β Low-Intermediate Frequency Band	< 0.001***	< 0.001***						
Latitude > 23.5° Vegetation Turnover β Low Frequency Band	< 0.001***	< 0.001***	< 0.001***					
Latitude > 23.5° TraCE-21ka Temperature β High Frequency Band	< 0.001***	0.008**	< 0.001***	< 0.001***				

Latitude > 23.5° TraCE-21ka Temperature β Low Frequency Band	< 0.001***	< 0.001***	< 0.001***	< 0.001***	< 0.001***			
Latitude > 23.5° TraCE-21ka Annual Precipitation Rate β High Frequency Band	< 0.001***	< 0.001***	< 0.001***	< 0.001***	< 0.001***	< 0.001***		
Latitude > 23.5° TraCE-21ka Annual Precipitation Rate β Low Frequency Band	< 0.001***	< 0.001***	< 0.001***	< 0.001***	< 0.001***	< 0.001***	< 0.001***	

Table S4

P-values of permutation tests comparing β for the extra-tropics from Fig. 3 where *** corresponds to values <0.001, ** indicates values between 0.001 and 0.01, and * indicates values between 0.01 and 0.05.

	Latitude > 23.5° Vegetation Turnover High Frequency Band - High-Intermediate Frequency Band Break Location	Latitude > 23.5° Vegetation Turnover High-Intermediate Frequency Band - Low-Intermediate Frequency Band Break Location	Latitude > 23.5° Vegetation Turnover Low-Intermediate Frequency Band - Low Frequency Band Break Location	Latitude > 23.5° TraCE-21ka Temperature High Frequency Band - Low Frequency Band Break Location	Latitude > 23.5° TraCE-21ka Annual Precipitation Rate High Frequency Band - Low Frequency Band Break Location
Latitude > 23.5° Vegetation Turnover High Frequency Band - High-Intermediate Frequency Band Break Location					
Latitude > 23.5° Vegetation Turnover High-Intermediate Frequency Band - Low-Intermediate Frequency Band Break Location	< 0.001***				
Latitude > 23.5° Vegetation Turnover Low-Intermediate Frequency Band - Low Frequency Band Break Location	< 0.001***	< 0.001***			
Latitude > 23.5° TraCE-21ka Temperature High Frequency Band - Low Frequency Band Break Location	< 0.001***	< 0.001***	< 0.001***		
Latitude > 23.5° TraCE-21ka Annual Precipitation Rate High Frequency Band - Low Frequency Band Break Location	< 0.001***	< 0.001***	< 0.001***	< 0.001***	

Table S5

P-values of permutation tests comparing break locations for the extra-tropics from Fig. 3 where *** corresponds to values <0.001, ** indicates values between 0.001 and 0.01, and * indicates values between 0.01 and 0.05.

	Latitude < 23.5° Vegetation Turnover High Frequency Band – Low Frequency Band Break Location	Latitude < 23.5° TraCE-21ka Temperature High Frequency Band - Low Frequency Band Break Location	Latitude < 23.5° TraCE-21ka Annual Precipitation Rate High Frequency Band - Low Frequency Band Break Location
Latitude < 23.5° Vegetation Turnover High Frequency Band – Low Frequency Band Break Location			
Latitude < 23.5° TraCE-21ka Temperature High Frequency Band - Low Frequency Band Break Location	< 0.001***		
Latitude < 23.5° TraCE-21ka Annual Precipitation Rate High Frequency Band - Low Frequency Band Break Location	< 0.001***	< 0.001***	

Table S6

P-values of permutation tests comparing break locations for the tropics from Fig. 3 where *** corresponds to values <0.001, ** indicates values between 0.001 and 0.01, and * indicates values between 0.01 and 0.05.

	Latitude < 23.5° Vegetation Turnover β High Frequency Band	Latitude < 23.5° Vegetation Turnover β Low Frequency Band	Latitude < 23.5° TraCE-21ka Temperature β High Frequency Band	Latitude < 23.5° TraCE-21ka Temperature β Low Frequency Band	Latitude < 23.5° TraCE-21ka Annual Precipitation Rate β High Frequency Band	Latitude < 23.5° TraCE-21ka Annual Precipitation Rate β Low Frequency Band
Latitude < 23.5° Vegetation Turnover β High Frequency Band						
Latitude < 23.5° Vegetation Turnover β Low Frequency Band	< 0.001***					
Latitude < 23.5° TraCE-21ka Temperature β High Frequency Band	< 0.001***	< 0.001***				
Latitude < 23.5° TraCE-21ka Temperature β Low Frequency Band	< 0.001***	< 0.001***	< 0.001***			
Latitude < 23.5° TraCE-21ka Annual Precipitation Rate β High Frequency Band	< 0.001***	< 0.001***	< 0.001***	< 0.001***		
Latitude < 23.5° TraCE-21ka Annual Precipitation Rate β Low Frequency Band	< 0.001***	< 0.001***	< 0.001***	< 0.001***	< 0.001***	

Table S7

P-values of permutation tests comparing β for the tropics from Fig. 3 where *** corresponds to values <0.001, ** indicates values between 0.001 and 0.01, and * indicates values between 0.01 and 0.05.

Site Name	Dataset ID	Failure Reason
Challa Lake	hXPNKEOsFdftFMmUvYYv	No age information in Temperature12k
Lake Malawi	Ff4CF5LsHToo394MMeFt	Not enough RAM for linterpLH13 interpolation algorithm
Midden Cluster 3	yCebthVVgiBnTTu63yvd	No resolvable frequencies determined by linterpLH13 interpolation algorithm
Midden Cluster 5	Mq5F6F6nmLYKNlACGome	No resolvable frequencies determined by linterpLH13 interpolation algorithm
Middel Cluster 6	39OKoIAcvAICa26B8Oiy	No resolvable frequencies determined by linterpLH13 interpolation algorithm
Soylegrotta	Ipsz1iUTCMtvZqRnxzs8	No resolvable frequencies determined by linterpLH13 interpolation algorithm

Table S8

Temperature12k sites that failed spectral analyses and the corresponding reason.

1687

Data S1 (separate file)

The list of sites considered in this study including those that were filtered out for issues with taxonomy harmonization, data quality (negative abundances), or chronological issues that prevented developing age models.